Electronic Structure of Linear Thiophenolate-Bridged Heterotrinuclear Complexes $[LFeMFeL]^{n+}$ (M = Cr, Co, Fe; $n = 1-3$): Localized vs Delocalized Models

Thorsten Glaser,[†] Thomas Beissel,[†] Eckhard Bill,[†] Thomas Weyhermüller,[†] Volker Schünemann,[‡] Wolfram Meyer-Klaucke,[§] Alfred X. Trautwein,[‡] and Karl Wieghardt*,[†]

Contribution from the Max-Planck-Institut für Strahlenchemie, D-45470 Mülheim and der Ruhr, Germany, Institut für Physik, Medizinische Universität, D-23538 Lübeck, Germany, and European Molecular Biology Laboratory, Outstation Hamburg, D-22603 Hamburg, Germany

Received August 12, 1998

Abstract: The reaction of mononuclear $[LFe^{III}]$ where L represents the trianionic ligand 1,4,7-tris(4-*tert*-butyl-2-mercaptobenzyl)-1,4,7-triazacyclononane with $CrSO_4 \cdot 5H_2O$, $CoCl_2 \cdot 6H_2O$, or $Fe(BF_4)_2 \cdot 6H_2O$ and subsequent oxidation with ferrocenium hexafluorophosphate or $NO(BF_4)$ or reduction with $[(tmcn)Mo(CO)_3]$ (tmcn = 1,4,7-trimethyl-1,4,7-triazacyclononane) produced an isostructural series of $[LFeMFeL]^{n+}$ complexes, the following salts of which were isolated as crystalline solids: (i) $[LFeCrFeL](PF_6)_n$ with $n = 1$ (**1a**), $n = 2$ (**1b**), and $n = 3$ (**1c**); (ii) $[LFeCoFeL]X_n$ with $X = BPh_4$ and $n = 2$ (**2b**) and $X = PF_6$ and $n = 3$ (**2c**); (iii) $[LFeFeFeL](BPh_4)_n$ with $n = 2$ (**3b**) and $n = 3$ (**3c**). All compounds contain linear trinuclear cations (face-sharing octahedral) with an $N_3Fe(\mu\text{-}SR)_3M(\mu\text{-}SR)_3FeN_3$ core structure. The electron structure of all complexes has been studied by Fe *and* M K-edge X-ray absorption near edge structure (XANES), UV−vis, and EPR spectroscopy, variable-temperature, variable-field susceptibility measurements, and Mössbauer spectroscopy (in zero and applied field). The following electronic structures have been established: (**1a**) $Fe^{II}(ls)Cr^{III}Fe^{II}(ls)$ (ls = low-spin) with a spin ground state of $S_t = {}^3/_2$; (**1c**) $Fe^{III}(ls)Cr^{III}Fe^{III}(ls)$ with an $S_t = {}^1/_2$ ground state; (**2c**) $Fe^{III}(ls)Co^{III}(ls)Fe^{III}(ls)$ with an $S_t = 1$ ground state; (**3c**) $Fe^{III}(ls)Fe^{III}(ls)Fe^{III}(ls)$ with an $S_t = {}^1/_2$ ground state. For **1b** ($S_t = 2$) it is found that the two iron ions are spectroscopically equivalent ($Fe^{2.5}$) and, therefore, the excess electron is delocalized (class III): $[LFe^{2.5}Cr^{III}Fe^{2.5}L]^{2+}$. For **2b** clearly two different iron sites prevail at low temperatures (4.2 K); at higher temperatures (>200 K) they become equivalent on the Mössbauer time scale. Thus, **2b** is class II with temperature-dependent electron hopping between the Fe^{II} and Fe^{III} ions. **3b** is again fully delocalized (class III) with an $S_t = 1$ ground state; the excess electron is delocalized over all three iron sites. The electronic structure of all complexes is discussed in terms of double exchange and superexchange mechanisms.

Introduction

Iron−sulfur metalloproteins are probably the structurally and spectroscopically most intensively studied class of metalloproteins.[1−5] These proteins contain active sites comprising tetrahedrally coordinated Fe^{II} and/or Fe^{III} ions and sulfido and S-bound cysteinato ligands. Mono-, di-, tri-, and tetranuclear core structures have been identified which exist in a variety of oxidation levels. The magnetic properties of these iron−sulfur clusters are well established.[6] High-spin d^6 and d^5 electronic configurations prevail in the Fe^{II} and Fe^{III} ions, respectively, which give rise to intramolecular antiferromagnetic exchange coupling in the dinuclear $[2Fe\text{-}2S]^{2+,1+}$ cores between either two Fe^{III} ions as in $[2Fe\text{-}2S]^{2+}$, yielding an $S_t = 0$ ground state, or between one Fe^{II} ion and one Fe^{III} ion in the mixed valent form $[2Fe\text{-}2S]^{1+}$ where both oxidation states are localized, affording an $S_t = {}^1/_2$ ground state. Interestingly, for the latter core an $S_t = {}^9/_2$ ground state has recently been shown to exist in a Cys 60 Ser mutant of *Clostridium pasteurianum* 2Fe ferredoxin.[7,8] Intramolecular antiferromagnetic coupling between three Fe^{III} ions in the oxidized form $[3Fe\text{-}4S]^{1+}$ yields an $S_t = {}^1/_2$ ground state.

In the mixed valent $[3Fe\text{-}4S]^0$ form of ferredoxin II of *Desulfovibrio gigas* comprising formally two Fe^{III} ions and one Fe^{II} ion, the valencies are delocalized. A $Fe^{2.5}{}_2$ pair with an $S^* = {}^9/_2$ state is antiferromagnetically coupled to one Fe^{III} ion ($S = {}^5/_2$), generating the observed $S_t = 2$ ground state of the trinuclear cluster.[9−11] The double exchange mechanism origi-

[†] Max-Planck-Institut für Strahlenchemie.
[‡] Medizinische Universität.
[§] European Molecular Biology Laboratory.

(1) *Iron−sulfur Proteins, Vol. I−III.;* Lovenberg, W., Ed.; Academic Press: New York, 1973−1977.
(2) *Iron−sulfur Clusters, Vol. IV.;* Spiro, T. G., Ed.; John Wiley & Sons: New York, 1982.
(3) *Advances in Inorganic Chemistry Vol. 38;* Cammack, R., Ed.; Academic Press: San Diego, 1992.
(4) Beinert, H. *FASEB J.* **1990**, *4*, 2483.
(5) Beinert, H.; Holm, R. H.; Münck, E. *Science* **1997**, *277*, 653.
(6) Trautwein, A. X.; Bill, E.; Bominaar, E. L.; Winkler, H. *Struct. Bonding* **1991**, *78*, 1.
(7) Crouse, B.; Meyer, J.; Johnson, M. K. *J. Am. Chem. Soc.* **1995**, *117*, 9612.
(8) Achim, C.; Colinelli, M.-P.; Bominaar, E. L.; Meyer, J.; Münck, E. *J. Am. Chem. Soc.* **1996**, *118*, 8168.
(9) Münck, E.; Kent, T. A. *Hyperfine Interact.* **1986**, *27*, 161.
(10) Papaefthymou, V.; Girerd, J.-J.; Moura, I.; Moura, J. J. G.; Münck, E. *J. Am. Chem. Soc.* **1987**, *109*, 4703.

10.1021/ja982898m CCC: $18.00
Published on Web 02/25/1999

nally introduced by Zener, Anderson, and Hasegawa[12,13] has been invoked to explain the spin alignment in the $Fe^{2.5}{}_2$ pair. In the cubane-type core structures $[4Fe\text{-}4S]^{3+,2+,1+}$ such a mixed valent $Fe^{2.5}{}_2$ pair with an $S^* = {}^9/_2$ state and delocalized excess electron occurs in all three oxidation levels. For example, the $S_t = 0$ ground state results from an antiferromagnetic coupling of two such pairs in the $[4Fe\text{-}4S]^{2+}$ cluster.

Remarkably, neither of these trinuclear or tetranuclear clusters exhibit in the ground state delocalization of the excess electron *over all three or four iron ions*. This observation has recently been rationalized by Girerd et al.[14−17] by taking into account vibronic coupling in the double exchange Hamiltonian which considers impeded electron transfer between tetrahedral high-spin Fe^{II} and high-spin Fe^{III} due to differing Fe−S bond lengths (large Franck−Condon barrier).

Accordingly, systems with small bond length differences between the oxidized and reduced forms should facilitate electron transfer and, consequently, electron delocalization. We have been inspired by the fact that the ionic radius of tetrahedrally coordinated Fe^{III} increases upon reduction to Fe^{II} by 22% which, in contrast, is only 9% for octahedrally coordinated low-spin Fe^{III} and Fe^{II}. Therefore, we investigated the electronic structures of sulfur-bridged, trinuclear complexes containing two terminal, octahedral Fe^{III}/Fe^{II} ions and a di- or trivalent central heterometal ion.

In this paper we present an isostructural series of heterotrinuclear thiophenolate-bridged complexes of the general formula $[LFeMFeL]^{n+}$ with M = Cr, Co, and Fe where L represents the trianionic form of the ligand 1,4,7-tris(4-*tert*-butyl-2-mercaptobenzyl)-1,4,7-triazacyclononane (Chart 1). In a recent publication[18] we discussed an analogous series containing nickel and cobalt ions. It was shown that the mechanism of spin coupling cannot be described exclusively in terms of the classical superexchange mechanisms but double exchange phenomena prevail.

This new series of complexes is uniquely suited to study the fine details of the electronic structure by Mössbauer spectroscopy in addition to the more conventional techniques such as temperature- and field-dependent magnetochemistry and multifrequency band EPR spectroscopy. We have also employed extended X-ray absorption fine structure (EXAFS) and X-ray absorption near edge structure (XANES) spectroscopy.

Experimental Section

General Procedures. All reagents and solvents were obtained from commercial sources and used as received unless noted otherwise. CH_2Cl_2 was distilled from calcium hydride under an oxygen-free, dry N_2 atmosphere. The preparations of all complexes were performed under an argon atmosphere by using standard Schlenck techniques. The ligands 1,4,7-triazacyclononane (tacn),[19] 1,4,7-trimethyl-1,4,7-triazacyclononane (tmcn),[20] and 1,4,7-tris(4-*tert*-butyl-2-mercaptobenzyl)-1,4,7-triazacyclononane (LH_3)[21] and the complexes [LFe][22] and $[(tmcn)Mo(CO)_3]$[23] were synthesized using published procedures.

Chart 1

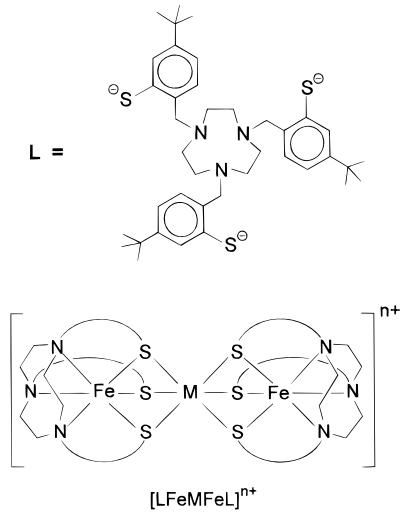

$[LFeMFeL]^{n+}$	n=1	S_t	n=2	S_t	n=3	S_t
Cr	**1a**	3/2	**1b**	4/2	**1c**	1/2
Co			**2b**	1/2	**2c**	2/2
Fe			**3b**	2/2	**3c**	1/2

Safety Note. ***Caution!*** *Perchlorate salts of metal complexes with organic ligands are potentially explosive. Only small amounts of material should be prepared, which should be handled with great care and appropiate precautions.*

Physical Methods. Infrared spectra (400−4000 cm^{-1}) of solid samples were recorded on a Perkin-Elmer 2000 FT-IR spectrometer (KBr disk). UV−vis/near-IR spectra of solutions were measured on a Perkin-Elmer Lambda 19 spectrophotometer in the range 210−3200 nm at ambient temperatures. Low-temperature spectra of substances in CsI disks were taken by mounting the disk in a holder attached to the end stage of an Air Products CS202 closed-cycle cryocooler. For infrared spectra the PE1760 FTIR was used, for UV−vis spectra the PE330 spectrometer, both computer controlled. Positive ion FAB mass spectra were obtained under the condition of liquid secondary ion mass spectrometry (L-SIMS) using Cs^+ as the primary ion (22 keV) on a VG autospectrometer with *m*-nitrobenzyl alcohol (MNBA) as the matrix solvent. Cyclic voltammetric and coulometric measurements were performed on EG & G equipment (potentiostat/galvanostat model 273A) on Ar-flushed acetonitrile solutions of samples containing 0.10 M $[N(n\text{-}but)_4]PF_6$ as supporting electrolyte under an argon blanketing atmosphere. Temperature- and magnetic field-dependent magnetic susceptibilities of powdered samples were measured by using a SQUID magnetometer (Quantum Design) at 1.0, 4.0, and 7 T, respectively (2.0−300 K). For calculations of the molar magnetic susceptibility, χ_M, the experimental susceptiblities were corrected for the underlying diamagnetism of the sample by using tabulated Pascal's constants and for the temperature-independent paramagnetism (χ_{TIP}) which was obtained by a fitting procedure. EPR spectra of frozen solutions and powdered solids

(11) Münck, E.; Papaefthymiou, V.; Surerus, K. K.; Girerd, J.-J. In *Double Exchange in Reduced Fe_3S_4 Clusters and Novel Clusters with MFe_3S_4 Cores*; Münck, E., Papaefthymiou, V., Surerus, K. K., Girerd, J.-J., Eds.; American Chemical Society: Washington, DC, 1988; Vol. 372.
(12) Zener, C. *Phys. Rev.* **1951**, *82*, 403.
(13) Anderson, P. W.; Hasegawa, H. *Phys. Rev.* **1955**, *100*, 675.
(14) Borshch, S. A.; Bominaar, E. L.; Girerd, J.-J. *New J. Chem.* **1993**, *17*, 39.
(15) Borshch, S. A.; Bominaar, E. L.; Blondin, G.; Girerd, J.-J. *J. Am. Chem. Soc.* **1993**, *115*, 5155.
(16) Bominaar, E. L.; Borshch, S. A.; Girerd, J.-J. *J. Am. Chem. Soc.* **1994**, *116*, 5362.
(17) Bominaar, E. L.; Hu, Z.; Münck, E.; Girerd, J.-J.; Borshch, S. A. *J. Am. Chem. Soc.* **1995**, *117*, 6976.
(18) Beissel, T.; Birkelbach, F.; Bill, E.; Glaser, T.; Kesting, F.; Krebs, C.; Weyhermüller, T.; Wieghardt, K.; Butzlaff, C.; Trautwein, A. X. *J. Am. Chem. Soc.* **1996**, *118*, 12376.
(19) Wieghardt, K.; Schmidt, W.; Nuber, B.; Weiss, J. *Chem. Ber.* **1979**, *112*, 2220.
(20) Wieghardt, K.; Chaudhuri, P.; Nuber, B.; Weiss, J. *Inorg. Chem.* **1982**, *21*, 3086.
(21) Beissel, T.; Glaser, T.; Kesting, F.; Wieghardt, K.; Nuber, B. *Inorg. Chem.* **1996**, *35*, 3936.
(22) Beissel, T.; Bürger, K. S.; Voigt, G.; Wieghardt, K. *Inorg. Chem.* **1993**, *32*, 124.
(23) Backes-Dahmann, G.; Herrmann, W.; Wieghardt, K.; Weiss, J. *Inorg. Chem.* **1985**, *24*, 485.

Chart 2

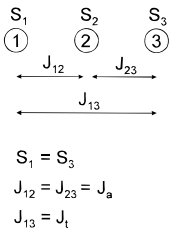

were recorded on a Bruker ESP 300E spectrometer equipped with a helium flow cryostat (X-band, Oxford Instruments ESR 910; S- and Q-band, Oxford Instruments CF935). The X-band resonator was a dual-mode cavity (Bruker ER4116DM/95). The Mössbauer spectra were recorded on an alternating constant-acceleration spectrometer. The minimal line width was 0.24 mm s^{-1} (full width at half-height). The sample temperature was maintained constant in either an Oxford Variox or an Oxford Mössbauer-Spectromag cryostat. The latter is a split-pair superconducting magnet system for applied fields up to 8 T where the temperature of the samples can be varied in the range 1.5−250 K. The field at the samples is oriented perpendicular to the γ-beam. The ^{57}-Co/Rh source (1.8 GBq) was positioned at room temperature inside the gap of the magnet system at a zero-field position. Isomer shifts are referenced relative to α-iron metal at 295 K.

Spin Hamiltonian Analysis. We have analyzed the data within the usual spin Hamiltonian formalism which includes a term for the electronic Hamiltonian, $\hat{H}_{el}$, and one for the nuclear Hamiltonian, $\hat{H}_N$, as in eq 1.[6,24] The electronic Hamiltonian takes into account the isotropic

$$\hat{H} = \hat{H}_{el} + \hat{H}_N \quad (1)$$

Heisenberg−Dirac−van Vleck exchange Hamiltonian ($\hat{H}_{HDvV}$), the intrinsic zero-field splitting terms ($\hat{H}_{ZVS}$), and the intrinsic electronic Zeeman terms ($\hat{H}_{Zee}$). For trinuclear complexes considered here the spin coupling model encompasses coupling between adjacent metal centers, J_a, and coupling between the terminal metal centers, J_t (Chart 2).[25−27] The electronic Hamiltonian is given in eq 2.

$$\hat{H}_{el} = -2J_a(\hat{\mathbf{S}}_1\hat{\mathbf{S}}_2 + \hat{\mathbf{S}}_2\hat{\mathbf{S}}_3) - 2J_t\hat{\mathbf{S}}_1\hat{\mathbf{S}}_3 + \sum_{i=1}^{3}\left\{D_i\left[\hat{S}_{z_i}^2 - \frac{1}{3}S_i(S_i+1) + \frac{E_i}{D_i}(\hat{S}_{x_i}^2 - \hat{S}_{y_i}^2)\right] + \mu_B\hat{\mathbf{S}}_i\bar{\bar{g}}_i\mathbf{B}\right\} \quad (2)$$

If the HDvV exchange term in eq 2 is dominant, the low-temperature spectroscopic measurements (i.e., EPR, Mössbauer, and magnetic measurements) can be simulated for an isolated ground spin manifold S_t. This is possible only if (i) the energy difference between the spin ground state and the first excited spin state is $\gg kT$ and (ii) the spin coupling dominates the zero-field splitting ($|J| \gg |D|$). The main factors affecting the energy of the system are then given by the effective electronic Hamiltonian $\hat{H}_{el}^{eff}$ (eq 3). The values of the effective spin

$$\hat{H}_{el}^{eff} = D\left[\hat{S}_{t,z}^2 - \frac{1}{3}S_t(S_t+1) + \frac{E}{D}(\hat{S}_{t,x}^2 - \hat{S}_{t,y}^2)\right] + \mu_B\hat{\mathbf{S}}_t\bar{\bar{g}}\mathbf{B} \quad (3)$$

Hamiltonian eq 3 (D, E, and $\bar{\bar{g}}$) are related to the intrinsic values in eq 2 (D_i, E_i, and $\bar{\bar{g}}_i$) by spin projection techniques.[28] The relevant expressions will be given in the text where applied.

The nuclear part of the spin Hamiltonian consists of the nuclear quadrupole interaction, the nuclear Zeeman terms, and the hyperfine coupling describing the interaction of the ground-state spin S_t (in the effective description) with the local nuclear moments (eq 4). The effective hyperfine tensor $\bar{\bar{A}}_i$ can also be converted to the intrinsic hyperfine tensor $\bar{\bar{a}}_i$ by spin projection techniques. The electronic and

$$\hat{H}_N = \sum_{i=1}^{3}\left\{\frac{eQV_{zz}}{12}[3\hat{I}_{z_i}^2 - I_i(I_i+1) + \eta(\hat{I}_{x_i}^2 - \hat{I}_{y_i}^2)] + \mu_N g_N\hat{\mathbf{I}}_i\mathbf{B} + \langle\mathbf{S}_t\rangle\bar{\bar{A}}_i\hat{\mathbf{I}}_i\right\} \quad (4)$$

the nuclear parts of the spin Hamiltonian are diagonalized separately because in an applied magnetic field electron and nuclear spins are decoupled. The Mössbauer spectra can be simulated in the limit either of fast or of slow spin relaxation. For the limit of fast spin relaxtion (i.e., the spin states fluctuate rapidly on the time scale of the nuclear frequencies due to spin−lattice and spin−spin relaxation) the spin expectation value $\langle\hat{\mathbf{S}}_t\rangle$ is thermally averaged over all populated spin states whereas for the limit of slow relaxation (i.e., the spin states fluctuate slowly on the time scale of the nuclear frequencies) a Mössbauer spectrum is the superposition of the Boltzmann-weighted spectra of all populated states.

X-ray Crystallographic Data Collection and Refinement of the Structures. A dark red-brown single crystal of [LFeCrFeL]$(ClO_4)_2$-(PF_6)·1 acetone (**1c***), a dark brown crystal of **2c**, and a black crystal of [LFeFeFeL]$(BPh_4)(BF_4)$·3 acetone (**3b***) were mounted in glass capillaries sealed under argon. Graphite-monochromated Mo Kα radiation ($\lambda = 0.710\ 73$ Å) was used throughout. Crystallographic data of the compounds and diffractometer types used are listed in Table 1. Cell constants for **1c*** and **2c** were obtained from a least-squares fit of the setting angles of 25 carefully centered reflections. Intensity data for these compounds were collected at 20(1) and −150(2) °C, respectively, by using the $\omega-2\theta$ scan technique, corrected for Lorentz and polarization effects, but no absorption correction was carried out due to small absorption coefficients. Compound **3b*** was measured on a Siemens SMART CCD-detector system at −173(2) °C. Cell constants were obtained from a subset of 4958 reflections. Data collection was performed by a hemisphere run taking frames at 0.30° in ω.

The Siemens ShelXTL[29a] software package was used for solution, refinement, and artwork of the structures. All structures were readily solved and refined by direct methods and difference Fourier techniques performed on DEC Alpha workstations. Neutral atom scattering factors were obtained from tables.[29b] All non-hydrogen atoms were refined anisotropically except those of a disordered *tert*-butyl group in **1c***, disordered solvent molecules, and some anions which were isotropically refined. All hydrogen atoms were placed at calculated positions and refined as riding atoms with isotropic displacement parameters. Some of the solvent molecules and anions in **1c***, **2c**, and **3b*** are disordered. For further information see the Supporting Information.

X-ray Absorption Spectroscopy (XAS). The XAS spectra were recorded at the beam lines E4 and X1.1 at HASYLAB (DESY, Hamburg, Germany). The beam lines are equipped with three ionization chambers, which allow a calibration of each spectrum according to a reference sample. The measurements were performed at room temperature. Monochromatization was achieved by a Si(111) monochromator for the Cr, Fe, and Co K-edges. At beam line E4 a focusing mirror is installed in front of the monochromator for further rejection of the harmonics. For the suppression of harmonics the monochromator has been detuned to 50% of its peak intensity. Energy calibration was achieved by use of reference samples. For the Fe K-edge an α-Fe foil, for the Co K-edge a Co foil, and for the Cr K-edge CrO_2-tape were chosen. The energy calibration of the data has been performed using WINXAS,[30a] whereas the normalization and data reduction were done with EXPROG,[30b] using a Victoreen function below the edge and three cubic splines above the edge. For the EXAFS analysis FEFF6/FEFFIT232[30c] was used. The edge positions were defined as the maximum of the first derivative in the rising edge. For samples with

(24) Rodriguez, J. H.; Ok, H. N.; Xia, Y.-M.; Debrunner, P. G.; Hinrichs, B. E.; Meyer, T.; Packard, N. H. *J. Phys. Chem.* **1996**, *100*, 6849.
(25) Sinn, E. *Coord. Chem. Rev.* **1970**, *5*, 313.
(26) Ginsberg, A. P. *Inorg. Chim. Acta Rev.* **1972**, *5*, 45.
(27) Griffith, J. S. *Struct. Bonding* **1972**, *10*, 87.
(28) Bencini, A.; Gatteschi, D. *Electron Paramagnetic Resonance of Exchanged Coupled Systems*; Springer-Verlag: Berlin, 1990.
(29) (a) ShelXTL V.5, Siemens Analytical X-ray Instruments, Inc., 1994. (b) *International Tables for X-ray Crystallography*; Kynoch Press: Birmingham, U.K. 1991.
(30) (a) Ressler, T., LLNL, EXAFS program for Windows 3 Version 2.4. http://ourworld.compuserve.com/homepage/tressler/. (b) Hermes, C.; Nolting, H. F., EMBL-Outstation Hamburg, Germany: *EXAFS data analysis and evaluation program package for PC*. (c) FEFF6: Zabinsky, S. I.; Rehr, J. J.; Ankudinov, A.; Albers, R. C.; Eller, M. J. *Phys. Rev.*, submitted for publication. FEFIT232: Newville, M.; Ravel, B.; Huskel, D.; Stern, E. A.; Yacoby, Y. *Physica B* **1995**, *208−209*, 154.

Table 1. Crystallographic Data of the Complexes

complex	**1c***·1 acetone	**2c**·2 acetone·6 acetonitrile	**3b***·3 acetone
chem formula	$C_{81}H_{114}Cl_2CrF_6Fe_2N_6O_9PS_6$	$C_{96}H_{138}CoF_{18}Fe_2N_{12}O_2P_3S_6$	$C_{111}H_{146}B_2F_4Fe_3N_6O_3S_6$
fw	1887.71	2290.08	2069.87
space group	$Pna2_1$	$P\bar{1}$	$P\bar{1}$
a, Å	20.488(4)	13.173(3)	15.403(3)
b, Å	17.890(4)	13.453(3)	16.474(3)
c, Å	25.116(5)	15.675(4)	22.935(4)
α, deg	90	104.10(3)	94.38(3)
β, deg	90	99.50(3)	94.36(3)
γ, deg	90	90.74(3)	91.61(3)
V, Å	9206(3)	2653(1)	5783(2)
Z	4	1	2
T, K	293(1)	100(2)	123(2)
radiation *λ*, Å	0.71073	0.71073	0.71073
ρ(calcd), g cm^{-3}	1.362	1.433	1.189
μ(Mo Kα), cm^{-1}	7.06	6.72	5.35
$R1^a$ [$I > 2\sigma(I)$]	0.063	0.065	0.101
$wR2^b$	0.167	0.173	0.235

[a] $R1 = \sum||F_o| - |F_c||/\sum|F_o|$, $R_w = [\sum w(|F_o| - |F_c|)^2/\sum wF_o^2]^{1/2}$ where $w = 4F_o^2/\sigma^2(F_o^2)$. [b] $wR2 = [\sum[w(F_o^2 - F_c^2)^2]/\sum[w(F_o^2)^2]]^{1/2}$ where $w = 1/\sigma^2(F_o^2) + (aP)^2 + bP$, $P = (F_o^2 + 2F_c^2)/3$.

similar edge shapes changes of the average oxidation state of the different metal atoms were readily deduced from a shift of the minimum of the second derivative in the rising edge.

Knowledge of the general structure of the compounds simplifies a detailed multiple scattering EXAFS analysis. Considering only statistical reasons, we would be able to optimize more than 20 parameters for each scan. To overcome the problem of high correlations between different parameters, we have used the simplest model possible. For the Co and Cr K-edges this includes only the contributions from the six sulfur atoms in the first shell, the back-scattering from the neighboring iron atoms, the very important multiple scattering contributions for the M−S−Fe−M path, and, even more importantly, the multiple scattering contributions within the first shell up to fourth order.

The local environment of the terminal iron atoms is not as symmetric as that of the central metal ion. Therefore, more parameters had to be included in the calculations. The first coordination sphere consists of sulfur and nitrogen atoms. The multiple scattering contributions within this shell are much smaller due to the lower symmetry compared to the central metal atom with its six sulfur ligands at similar distances. The larger average distances of these sulfur ligands result in a contribution of the multiple scattering within the first coordination sphere at 3.9 Å for the Co K-edge, whereas the corresponding contribution for the Fe K-edge is at 3.7 Å. The fit of these peaks is not perfect because additional contributions from single scattering of several carbon atoms at distances >4 Å were not included in the refinement (carbon atoms of the macrocyclic ligand at ∼3 Å were).

The measurements on the terminal and central metal atoms contain the same information about the metal−metal distance and its disorder. Hence, this information can be extracted with much higher accuracy if both measurements are refined simultaneously. Thus, we have used a multiple edge fit in the refinements, which implies the use of the same parameter for the Fe−M distance and its Debye−Waller parameter, respectively. *The higher accuracy obtained with this approach allows analysis of whether the Fe atoms in the mixed valent samples have different distances to the central metal atom.* It is also possible to split the Debye−Waller parameter, but this did not improve the quality of the fit. The values obtained by both approaches were identical within the error bars. The results of this fitting procedure are available in Table S16 in the Supporting Information.

Preparation of Complexes. **[LFeCrFeL](PF$_6$) (1a).** To a stirred solution of 0.30 g (0.42 mmol) of [LFe] in methanol (50 mL) was added 0.30 g of $Cr^{II}SO_4 \cdot 5H_2O$ (1.26 mmol). The mixture was heated to reflux for 7 h, during which time the color changed from green-blue to light green. After cooling to room temperature, the solution was filtered. Addition of a solution of 0.50 g of $NaPF_6$ in methanol (20 mL) initiated after storage overnight at 4 °C the deposition of a green powder. Yield: 0.08 g, 23%. L-SIMS (MNBA) *m*/*z* (rel intens): 1629 {[LFeCrFeL](PF$_6$)$^+$, 4}; 1484 {[LFeCrFeL]$^+$, 53}; 788 {[LFeCrF]$^+$, 14}; 742; {[LFeCrFeL]$^{2+}$, 40}. Anal. Calcd for $C_{78}H_{108}N_6S_6PF_6Fe_2Cr$: C, 57.4; H, 6.7; N, 5.1; S, 11.8; Fe, 6.8; Cr, 3.2. Found: C, 56.9; H, 6.8; N, 4.8; S, 12.2; Fe, 6.3; Cr, 3.1.

[LFeCrFeL](PF$_6$)$_2$ (1b). To a stirred solution of 0.15 g (0.078 mmol) of **1c** in CH_3CN (15 mL) was added solid [(tmcn)Mo(CO)$_3$] (0.03 mg, 0.086 mmol). The mixture was heated to reflux for 1.5 h. The initially deep red-brown solution became deep green-brown. The solution was filtered and the filtrate treated with a filtered solution of 1.00 g of $NaPF_6$ in CH_3CN (10 mL). Upon storage of this solution overnight at 4 °C black crystals precipitated.Yield: 0.11 g (80%). L-SIMS (MNBA) *m*/*z* (rel intens): 1774 {[LFeCrFeL](PF$_6$)$_2^+$, 1}; 1629 {[LFeCrFeL](PF$_6$)$^+$, 8}; 1503 {[LFeCrFeL](F)$^+$, 11}; 1484 {[LFeCrFeL]$^+$, 42}; 742 {[LFeCrFeL]$^{2+}$, 39}. Anal. Calcd for $C_{78}H_{108}N_6S_6P_2F_{12}Fe_2Cr$: C, 52.8; H, 6.1; N, 4.7; S, 10.8. Found: C, 53.0; H, 6.9; N, 4.9; S, 10.3.

[LFeCrFeL](PF$_6$)$_3$ (1c). To a stirred solution of 0.30 g (0.42 mmol) of [LFe] in methanol (50 mL) was added 0.30 g of $Cr^{II}SO_4 \cdot 5H_2O$ (1.26 mmol). The mixture was heated at reflux for 5 h. The color changed from green-blue to light green. After cooling to room temperature, air was bubbled through the solution for 1 h. After addition of 0.14 g of $FcPF_6$ (0.42 mmol) the solution was heated at reflux for 2 h, after which time a deep red-brown solution was obtained. A filtered solution of 0.50 g of $NaPF_6$ in methanol (20 mL) was added. Storage of this solution overnight at 4 °C produced black crystals. Yield: 0.31 g, 77%. L-SIMS (MNBA) *m*/*z* (rel intens): 1774 {[LFeCrFeL](PF$_6$)$_2^+$, 1}; 1629 {[LFeCrFeL](PF$_6$)$^+$, 4}; 1484 {[LFeCrFeL]$^+$, 15}; 787 {[LFeCrF]$^+$, 13}; 742 {[LFeCrFeL]$^{2+}$, 39}. Anal. Calcd for $C_{78}H_{108}N_6S_6P_3F_{18}Fe_2Cr$: C, 48.8; H, 5.7; N, 4.4; S, 10.0. Found: C, 48.4; H, 5.9; N, 4.2; S, 9.8.

[LFeCoFeL](BPh$_4$)$_2$ (2b). To a stirred solution of 0.13 g (0.067 mmol) of **2c** in CH_3CN (50 mL) was added solid [(tmcn)Mo(CO)$_3$] (0.024 g, 0.067 mmol). The mixture was heated at reflux for 1 h. After cooling to room temperature, the solution was filtered, and a filtered solution of 0.50 g of $NaBPh_4$ in CH_3CN (20 mL) was added to the filtrate, which initiated the deposition of black microcrystals. Yield: 0.11 g (73%). L-SIMS (MNBA) *m*/*z* (rel intens): 1810 {[LFeCoFeL](BPh$_4$)$^+$, 0.2}; 1491 {[LFeCoFeL]$^+$, 9}; 775 {[LFeCo]$^+$, 8}; 745 {[LFeCoFeL]$^{2+}$, 7}; 716 {[LFe]$^+$, 4}. Anal. Calcd for $C_{126}H_{148}N_6S_6B_2Fe_2Co$: C, 71.0; H, 7.0; N, 3.9; S, 9.0. Found: C, 70.9; H, 7.0; N, 3.6; S, 8.7.

[LFeCoFeL](PF$_6$)$_3$ (2c). To a stirred solution of 0.30 g (0.42 mmol) of [LFe] in methanol (50 mL) was added 0.10 g of $Co^{II}Cl_2 \cdot 6H_2O$ (0.42 mmol). The mixture was heated at reflux for 1 h. After cooling to room temperature, air was bubbled through the solution for 1 h. After addition of 0.14 g of $FcPF_6$ (0.42 mmol) and CH_3CN (20 mL) the solution was heated at reflux for 1 h. After cooling to room temperature, the solution was filtered. Addition of a filtered solution of 0.50 g of $NaPF_6$ in acetone (20 mL) and slow evaporation of the solvent caused the precipitation of large black crystals. Yield: 0.27 g, 67%. L-SIMS (MNBA) *m*/*z* (rel intens): 1782 {[LFeCoFeL](PF$_6$)$_2^+$, 1}; 1636 {[LFeCoFeL](PF$_6$)$^+$, 3}; 1491 {[LFeCoFeL]$^+$, 7}; 775 {[LFeCo]$^+$, 6}; 745 {[LFeCoFeL]$^{2+}$, 39};

716 {[LFe]$^+$, 11}. Anal. Calcd for $C_{78}H_{108}N_6S_6P_3F_{18}Fe_2Co$: C, 48.6; H, 5.6; N, 4.3; S, 10.1. Found: C, 47.3; H, 6.2; N, 4.0; S, 9.8.

[LFeFeFeL](BPh$_4$)$_2$ (3b). To a stirred solution of 0.40 g (0.56 mmol) of [LFe] in acetone (30 mL) was added [Fe(H$_2$O)$_6$](BF$_4$)$_2$ (0.196 g, 0.56 mmol). The color changed from blue-green to olive-green. The mixture was heated at reflux for 1 h. After cooling to room temperature, the mixture was filtered, and a filtered solution of 0.50 g of NaBPh$_4$ in acetone (10 mL) was added. Upon storage at −18 °C black microcrystals were obtained. The solid was redissolved in CH$_3$CN (40 mL) with an excess of ascorbic acid (3.00 g). The mixture was heated at reflux for 2 h. The color changed from brown-green to olive-green. After cooling to room temperature, the mixture was filtered, and a filtered solution of 0.50 g of NaBPh$_4$ in acetone (10 mL) was added. Upon storage at −18 °C black crystals were obtained. Yield: 0.21 g, 50%. L-SIMS (MNBA) *m/z* (rel intens): 1808 {[LFeFeFeL](BPh$_4$)$^+$, 0.1}; 1488 {[LFeFeFeL]$^+$, 6}; 772 {[LFeFe]$^+$, 5}; 744 {[LFeFeFeL]$^{2+}$, 7}; 716 {[LFe]$^+$, 2}. Anal. Calcd for $C_{126}H_{148}N_6S_6B_2Fe_3$: C, 71.1; H, 7.0; N, 3.9; S, 9.0; Fe, 7.9. Found: C, 70.9; H, 7.3; N, 3.7; S, 9.3; Fe, 7.8.

[LFeFeFeL](BPh$_4$)$_3$ (3c). To a stirred solution of 0.30 g (0.42 mmol) of [LFe] in acetone (30 mL) was added [Fe(H$_2$O)$_6$](BF$_4$)$_2$ (0.141 g, 0.42 mmol). The color changed from blue-green to olive-green. The mixture was heated at reflux for 1 h. After cooling to room temperature, solid NOBF$_4$ (0.05 g, 0.42 mmol) was added to the solution, which was gently heated to 40 °C for 2 h. To the cooled and filtered solution was added a filtered solution of 0.50 g of NaBPh$_4$ in acetone (10 mL). Upon storage at −18 °C overnight black crystals were obtained.Yield: 0.30 g, 60%. L-SIMS (MNBA) *m/z* (rel intens): 1808 {[LFeFeFeL](BPh$_4$)$^+$, 1}; 1489 {[LFeFeFeL]$^+$, 6}; 744 {[LFeFeFeL]$^{2+}$, 15}; 716 {[LFe]$^+$, 2}. Anal. Calcd for $C_{150}H_{168}N_6S_6B_3Fe_3$: C, 73.6; H, 6.9; N, 3.4; S, 7.9; Fe, 6.9. Found: C, 73.5; H, 7.2; N, 3.3; S, 7.4; Fe, 7.1.

Results

Synthesis of Complexes. The preparation and crystal structure of the mononuclear starting material blue-green, mononuclear [LFe^{III}] have been recently described.[22] The iron(III) ion is coordinated in an octahedral *cis*-N$_3$S$_3$ donor environment. We have employed the following compounds as effective one-electron oxidants: ferrocenium hexafluorophoshate, [Fc]PF$_6$, or nitrosyl tetrafluoroborate, NOBF$_4$. [(1,4,7-Trimethyl-1,4,7-triazacyclononane)tricarbonylchromium(0)],[23] [(tmcn)Mo(CO)$_3$],[23] and ascorbic acid were used as one-electron reductants.

From the reaction of [LFe^{III}] with Cr^{II}SO$_4$·5H$_2$O (1:3) in methanol under anaerobic conditions green microcrystals of [LFeCrFeL](PF$_6$) (**1a**) were obtained. The chromium(II) salt was used in excess because it not only is the source for the central chromium in **1a** but also serves also as a one-electron reductant. From the above reaction mixture the two-electron-oxidized form [LFeCrFeL](PF$_6$)$_3$ (**1c**) was isolated as red-brown crystals by exposing the reaction mixture to oxygen (air) and adding 2 equiv of [Fc]PF$_6$. Generation of the intermediate oxidation state, namely, green-brown [LFeCrFeL](PF$_6$)$_2$ (**1b**), was achieved by reduction of the trication **1c** with 1 equiv of [(tmcn)Mo(CO)$_3$] in acetonitrile. The cations in **1a**, **1b**, and **1c** differ only in the total charge *n* ranging from $n = 1$ for **1a** to $n = 2$ for **1b** to $n = 3$ for **1c**. As we show below the formal oxidation state of the chromium center is +3 in all three cations. If this is the case, the terminal iron centers in **1a** and **1c** comprise homovalent Fe^{II}Fe^{II} and Fe^{III}Fe^{III} pairs, respectively, whereas **1b** contains a mixed valent Fe^{II}Fe^{III} pair.

The corresponding trinuclear unit with a cobalt ion in the central position is assembled similarly by the reaction of [LFe^{III}] with Co^{II}Cl$_2$·6H$_2$O in methanol. Air was bubbled through the reaction solution in order to oxidize the cobalt(II) ions. The resulting solution consists of a mixture of the dication [LFeCoFeL]$^{2+}$ and the trication [LFeCoFeL]$^{3+}$. The pure trication was obtained by adding 1 equiv of [Fc]PF$_6$. From the brown solution [LFeCoFeL](PF$_6$)$_3$ (**2c**) precipitated. Reduction of **2c** with 1 equiv of [(tmcn)Mo(CO)$_3$] in acetonitrile under anaerobic conditions yields the dication [LFeCoFeL](BPh$_4$)$_2$ (**2b**). The central cobalt ion is assigned a +3 oxidation state in both **2b** and **2c**; the trication in **2c** contains then a homovalent Fe^{III}Fe^{III} pair whereas in **2b** a mixed valent Fe^{II}Fe^{III} pair is present.

Analogously, the reaction of [LFe^{III}] with Fe^{II}BF$_4$·6H$_2$O in acetone yields the trinuclear unit with an iron ion in the central position. Again, the reaction solution contains the di- and tricationic forms. Addition of NOBF$_4$ yields a brown solution from which, upon addition of NaClO$_4$, brown crystals of [LFeFeFeL](ClO$_4$)$_3$ (**3c**) were obtained. By refluxing a mixture of the di- and trications in acetonitile in the presence of a large excess of ascorbic acid as the reducing agent, the pure dication [LFeFeFeL]$^{2+}$ formed in quantitative yield. From the olive-green solution, crystals of [LFeFeFeL](BPh$_4$)$_2$ (**3b**) precipitated. In the trication it appears to be natural that all three iron ions are assigned a +3 oxidation state. It is not possible at this point to assign local oxidation states of the iron ions in the dication **3b**, except to note that formally two iron ions are ferric ions and one is a ferrous ion.

Table 2. Electrochemical Data of the Complexes[a]

	redox potential *E*, V vs Fc$^+$/Fc			
complex	4+/3+[b]	3+/2+[b]	2+/1+[b]	1+/0[b]
1b[c]	+1.22 (r)	−0.23 (r)	−0.67 (r)	−1.99 (ir)
2c[c]	+1.03 (r)	−0.23 (r)	−0.83 (r)	−1.50 (ir)
3c[d]	+0.98 (ir)	−0.14 (r)	−0.95 (ir)	

[a] Conditions: acetonitrile solution; 0.10 M tetra-*n*-butylammonium hexafluorophosphate supporting electrolyte; ferrocene (10^{-3} M) as internal reference; 295 K; glassy carbon working electrode; Ag/AgCl (saturated LiCl in C$_2$H$_5$OH); r = reversible ($E = E_{1/2} = (E_p(ox) + E_p(red))/2$); ir = irreversible ($E = E_p(ox)$ or $E_p(red)$. [b] Charge of the complex couple. [c] Scan rate 200 mV s^{-1}. [d] Scan rate 100 mV s^{-1}.

Electrochemistry. The results of the electrochemical investigations are summarized in Table 2. All redox potentials are referenced in volts versus the ferrocenium/ferrocene couple (Fc$^+$/Fc).

The cyclic voltammograms (CV) of all trinuclear complexes display in the potential range +1.5 to −1.3 V in acetonitrile (0.10 M [N(*n*-butyl)$_4$]PF$_6$) up to *three* reversible one-electron transfer waves (Figure S1 in the Supporting Information) where the CVs are identical within a given series (**1a**, **1b**, and **1c**; **2b** and **2c**; and **3b** and **3c**). These processes correspond to the couples [LFeMFeL]$^{(n+1)/n+}$, i.e., 4+/3+, 3+/2+, and 2+/1+. The 1+/0 couple is irreversible for all complexes; it is not observed in the above potential range for **3b** and **3c** because at the 2+/1+ reduction level dissociation of the trinuclear unit occurs. The 3+/2+ couple is reversible on the time scale of CV and potentiostatic coulometry experiments. Thus, the di- and tricationic species [LFeMFeL]$^{3+/2+}$ (M = Cr, Co, Fe) are stable in solution and are chemically accessible.

In contrast, the 4+/3+ couple is reversible only for M = Cr and Co complexes, but on the time scale of a coulometric experiment the respective tetracations are not stable. The [LFeFeFeL]$^{4+}$ species is unstable even on the time scale of a cyclic voltammetric experiment; the 4+/3+ wave is irreversible. Thus, no tetracationic complex has been isolated in the solid state. Similarly, the 2+/1+ process is reversible only for the M = Cr and Co series on the time scale of a CV experiment; it is irreversible for **3b** and **3c**. On the time scale of a coulometric experiment [LFeMFeL]$^{1+}$ species with M = Co and Fe are also unstable. They dissociate with formation of mononuclear [LFe],

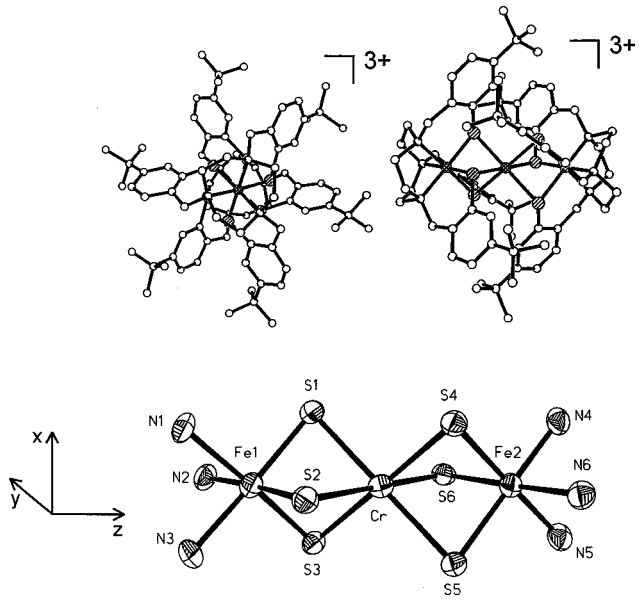

Figure 1. Structure of the trication in crystals of $[LFeCrFeL](ClO_4)_2$-$(PF_6)\cdot$(acetone) (**1c***). Top left: perspective view down the Fe−Cr−Fe axis emphasizing the staggered configuration of the six μ_2-thiophenolato bridges. Top right: side view of the trication. Bottom: first coordination sphere of the metal ions of the trication and molecular coordinate system used throughout.

the CV of which[22] is detected upon repetitive scanning. In contrast, $[LFeCrFeL]^{1+}$ is stable and has been isolated as complex **1a**.

Solid-State Molecular Structures of $[LFeCrFeL](ClO_4)_2$-$(PF_6)\cdot$Acetone (1c*), $[LFeCoFeL](PF_6)_3\cdot 6CH_3CN\cdot 2$ Acetone (2c), and $[LFeFeFeL](BPh_4)(BF_4)\cdot 3$ Acetone (3b*). The crystal structures of **1c***, **2c**, and **3b*** consist of trinuclear cations $[LFeM_cFeL]^{n+}$, well-separated anions, and solvent molecules. Figure 1 displays the structure of the trication $[LFeCrFeL]^{3+}$ representative of these trinuclear cations which possess idealized S_6 symmetry. Considering the metal centers within their respective first coordination sphere only, idealized D_{3d} symmetry prevails. The terminal iron centers are in a distorted octahedral *cis*-N_3S_3 coordination environment whereas the central metal ions are in a distorted octahedral S_6 donor atom coordination sphere. The stereochemistry of these trinuclear cations has been discussed previously.[18] Only the staggered configuration of the tertiary butyl groups in the achiral stereoisomer $\Delta(\lambda\lambda\lambda)\cdots\Lambda$-$(\delta\delta\delta)$ leads to a stable, sterically not crowded structure. Thus, for all complexes of the $[LM_tM_cM_tL]^{n+}$ type only one achiral stereoisomer needs to be considered. This is in contrast to similar complexes containing the less bulky aminoethanethiolate (aet) ligand as in $[(aet)_3Co^{III}Co^{III}Co^{III}(aet)_3]^{3+}$, three stereoisomer of which have been synthesized and characterized.[31−34]

Table 3 summarizes selected bond distances and angles of the $N_3Fe(\mu\text{-}S)_3M_c(\mu\text{-}S)_3FeN_3$ core. The short average Fe_t-N bond distances of 2.055(10), 2.038(3), and 2.059(8) Å in **1c***, **2c**, and **3b***, respectively, in comparison with 2.03 Å in low-spin (ls) $[(tacn)_2Fe^{II}](Cl)_2$,[35] with 1.99 Å in ls $[(tacn)_2Fe^{III}](Cl)_3$,[35] and with 2.24 Å in high-spin (hs) $[L^0Fe^{III}]$[36] indicate that the iron centers irrespective of their actual oxidation state adopt a low-spin electron configuration. The average Fe−S bond distances confirm this assignment. Published Fe−S bond distances for octahedrally coordinated iron ions with at least three sulfur ligands are found in the range 2.26−2.34 Å for ls Fe^{II},[37−52] 2.23−2.36 Å for ls Fe^{III},[46,53−58] 2.51−2.57 Å for hs Fe^{II},[39,41,53,59−64] and 2.57 Å for hs Fe^{III}.[65]

Table 3. Selected Average Bond Distances (Å) and Angles (deg) of the Trication $[LFeCrFeL]^{3+}$ in Crystals of **1c***, of the Trication $[LFeCoFeL]^{3+}$ in **2c**, and of the Dication $[LFeFeFeL]^{2+}$ in **3b*** Determined by X-ray Crystallography

	1c*	2c	3b*
Fe_t-N	2.055(10)	2.038(3)	2.059(8)
Fe_t-S	2.257(3)	2.234(1)	2.236(3)
M_c-S	2.398(3)	2.286(1)	2.297(2)
$Fe_t\cdots M_c$	2.941(3)	2.870(1)	2.848(2)
Fe_t-S-M_c	78.30(10)	78.82(4)	77.81(8)

(31) (a) Konno, T.; Aizawa, S.; Okamoto, K.; Hikada, J. *Chem. Lett.* **1985**, 1017. (b) Okamoto, K.; Aizawa, S.; Konno, T.; Einaga, H.; Hidaka, J. *Bull. Chem. Soc. Jpn.* **1986**, *59*, 3859. (c) Aizawa, S.; Okamoto, K.; Einaga, H.; Hikada, J. *Bull. Chem. Soc. Jpn.* **1988**, *61*, 1601.

(32) Miyanowaki, S.; Konno, T.; Okamoto, K.; Hidaka, J. *Bull. Chem. Soc. Jpn.* **1988**, *61*, 2987.

(33) Konno, T.; Aizawa, S.; Hidaka, J. *Bull. Chem. Soc. Jpn.* **1989**, *62*, 585.

(34) Konno, T.; Aizawa, S.; Okamoto, K.; Hidaka, J. *Bull. Chem. Soc. Jpn.* **1990**, *63*, 792.

(35) Boyens, U.; Forbes, A. G. S.; Hancock, R. D.; Wieghardt, K. *Inorg. Chem.* **1985**, *21*, 2926.

(36) Auerbach, U.; Eckert, U.; Wieghardt, K.; Nuber, B.; Weiss, J. *Inorg. Chem.* **1990**, *29*, 938.

(37) Sellmann, D.; Lanzrath, G.; Huttner, G.; Zsolnai, L.; Krüger, C.; Claus, K. H. *Z. Naturforsch., Teil B* **1983**, *38*, 961.

(38) Sellmann, D.; Jonk, H.-E.; Pfeil, H.-R.; Huttner, G.; Seyerl, J. *J. Organomet. Chem.* **1980**, *191*, 171.

(39) Berger, U.; Strähle, J. *Z. Anorg. Allg. Chem.* **1984**, *516*, 19.

(40) Wieghardt, K.; Küppers, H.-J.; Weiss, J. *Inorg. Chem.* **1985**, *24*, 3067.

(41) Walters, M. A.; Dewan, J. C. *Inorg. Chem.* **1986**, *25*, 4889.

(42) Küppers, H.-J.; Wieghardt, K.; Nuber, B.; Weiss, J.; Bill, E.; Trautwein, A. X. *Inorg. Chem.* **1987**, *26*, 3762.

(43) Sellmann, D.; Mahr, G.; Knoch, F.; M., M. *Inorg. Chim. Acta* **1994**, *224*, 45.

(44) Sellmann, D.; Weiss, R.; Knoch, F.; Ritter, G.; Dengler, J. *Inorg. Chem.* **1990**, *29*, 4107.

(45) Treichel, P. M.; Crane, R. A.; Matthews, R.; Bonnin, K. R.; Powell, D. *J. Organomet. Chem.* **1991**, *402*, 233.

(46) Atkinson, N.; Lavery, A. J.; Blake, A. J.; Reid, G.; Schröder, M. *Polyhedron* **1990**, *9*, 2641.

(47) Grant, G. J.; Isaac, S. M.; Setzer, W. N.; Vann Derveer, D. G. *Inorg. Chem.* **1993**, *32*, 4284.

(48) Sellmann, D.; Becker, T.; Knoch, F. *Chem. Eur. J.* **1996**, *2*, 1092.

(49) Ge, P.; Haggerty, B. S.; Rheingold, A. L.; Riordan, C. G. *J. Am. Chem. Soc.* **1990**, *116*, 8406.

(50) Sellmann, D.; Becker, T.; Knoch, F. *Angew. Chem., Int. Ed. Engl.* **1989**, *28*, 1703.

(51) Sellmann, D.; Mahr, G.; Knoch, F. *Angew. Chem., Int. Ed. Engl.* **1991**, *39*, 1477.

(52) Ohrenberg, C.; Ge, P.; Schebler, P.; Riordan, C. G.; Yap, G. P. A.; Rheingold, A. L. *Inorg. Chem.* **1996**, *35*, 749.

(53) Wolff, T. E.; Berg, J. M.; Power, P. P.; Hodgson, K. O.; Holm, R. H. *Inorg. Chem.* **1980**, *19*, 430.

(54) Henkel, G.; Simon, W.; Strasdeit, H.; Krebs, B. *Inorg. Chim. Acta* **1983**, *70*, 29.

(55) Greaney, M. A.; Coyle, C. L.; Pilato, R. S.; Stiefel, E. I. *Inorg. Chim. Acta* **1991**, *189*, 81.

(56) Hildebrand, U.; Lex, J.; Taraz, K.; Winkler, S.; Ockels, W.; Budzikiewicz, H. *Z. Naturforsch., Teil B* **1984**, *39*, 1607.

(57) Beckett, R.; Heath, G. A.; Hoskins, B. F.; Kelley, B. P.; L., M. R.; Roos, I. A. G.; Weickard, P. L. *Inorg. Nucl. Chem. Lett.* **1970**, *6*, 257.

(58) Blake, A. J.; Holder, A. J.; Hyde, T. I.; Schröder, M. *J. Chem. Soc., Chem. Commun.* **1989**, 1433.

(59) Beisheng, K.; Jinhua, C.; Changneng, C.; Jiaxi, L. *Acta Chim. Sin.* **1986**, *44*, 181.

(60) Latham, I. A.; Leigh, G. J.; Pickett, C. J.; Huttner, G.; Jibrill, I.; Zubeita, J. *J. Chem. Soc., Dalton Trans.* **1986**, 1181.

(61) Rosenfield, S. G.; Swedberg, S. A.; Arora, S. L.; Mascharak, P. K. *Inorg. Chem.* **1986**, *25*, 2109.

(62) Rosenfield, S. G.; Mascharak, P. K.; Arora, S. L. *Inorg. Chim. Acta* **1987**, *129*, 39.

(63) Nefedov, S. E.; Pasynskii, A. A.; Ermenko, I. L.; Gasanov, G. S.; Ellert, O. G.; Novotortsev, V. M.; Yanovsky, I.; Struchkov, Y. T. *J. Organomet. Chem.* **1993**, *443*, 101.

(64) Kang, B.; Liu, H.; Cai, J.; Huang, L.; Liu, Q.; Wu, D.; Weng, L.; Lu, J. *Trans. Met. Chem.* **1989**, *14*, 427.

The average Cr−S distance of 2.398 Å in **1c*** corresponds nicely to the average value of 2.40 Å for a Cr^{III}−S bond in octahedral $Cr^{III}S_6$ compounds.[66−69] Similarly, the Co−S distance of 2.286 Å in **2c** corresponds to an average of 2.27 Å for a Co^{III}−S bond distance in other octahedral $Co^{III}S_6$ compounds.[31b,70−74]

EXAFS and XANES Spectroscopy. We have measured the EXAFS spectra of complexes **1a**, **1b**, **1c**, **2b**, and **2c** at the Fe, Cr, and Co K-edges at ambient temperatures. The results are summarized in Table S16. Figures of the experimental and fitted *k* and *R* space data are available in the Supporting Information (Figures S2, S3, and S4).

An important aspect for the elucidation of the electronic structure of the trinuclear cations is the determination of the $Fe_t\cdots M_c$ metal−metal distances and the Fe_t−N, Fe_t−S, and M_c−S bond distances as a function of the oxidation level $n+$ within a given $[LFeMFeL]^{n+}$ series. Furthermore, an important issue concerns the question of whether the two terminal Fe ions in the mixed valent species **1b** and **2b** are equivalent, and if the latter is true whether one can distinguish the two iron ions by EXAFS spectroscopy.

The results in Tables 3 and S16 show that the $Fe_t\cdots M_c$, Fe_t−N, Fe_t−S, and M_c−S distances for **1c*** and **2c** as determined by X-ray crystallography are in excellent accord with those determined by EXAFS spectrocopy. This successful calibration gives us confidence that the theoretical phases used in the calculations are appropriate.[75]

It is therefore significant that the Fe_t−N and Fe_t−S bond lengths in **1a**, **1b**, **1c**, **2b**, and **2c** are within experimental error the same. They do not vary significantly as a function of the oxidation level within a series or the nature of the central ion (Cr or Co). The same is true for the M_c−S distances in **1a**, **1b**, and **1c** where the average Cr−S distance is 2.401(4) Å and in **2b** and **2c** with an average Co−S distance of 2.285(10) Å. Again, both M_c−S distances agree nicely with the corresponding values obtained from X-ray crystallography for **1c*** and **2c**.

The only parameter that does vary with the oxidation level is the $Fe_t\cdots M_c$ distance which is 3.07(1) Å in **1a** but 2.97(3) in **1c**. Since we have established by two different fitting procedures that the two iron ions in the mixed valent species $[LFeCrFeL]^{2+}$ (**1b**) are equivalent, it is gratifying that the single $Fe_t\cdots Cr$ distance of 3.01(1) Å is intermediate between that of **1a** and **1c**.

On the other hand, the same procedure has established that the two iron sites in $[LFeCoFeL]^{2+}$ (**2b**) are *not* equivalent, and two different $Fe_t\cdots Co$ distances at 2.80(3) and 3.02(5) Å have been determined. We regard this as a very important result of the EXAFS spectra that the mixed valent species **1b** contains two, on the EXAFS time scale (10^{-15} s), equivalent iron ions whereas in **2b** they are different.

We have also attempted to analyze the Fe K-edge EXAFS spectra of **3b** and **3c**. These spectra represent a superposition of the contributions arising from the two Fe_t and Fe_c ions. The system is overparametrized, and therefore, the standard deviations are large. The only significant result obtained is an $Fe_t\cdots Fe_c$ distance of 2.99(3) Å in **3b** and 2.86(2) Å in **3c**. Again, the $Fe_t\cdots M$ distance decreases with increasing oxidation level.

XAS as an element specific spectroscopy allows the oxidation state of a given element in a coordination compound to be analyzed. The position and intensity of the resonances and, in particular, the energy of the absorption edge position are features which depend on the d^n electron configuration. We have determined the edge positions from the maximum of the first derivative of the data in the rising edge region.[76−78] Resonances from the 1s level into half-occupied and/or empty d or p orbitals give rise to distinct features superimposed on the K-edge transitions. We have not attempted to assign these transitions in any detail but use the energies listed in Table S17 in a qualitative fashion.

The three Fe K-edge XAS spectra of **1a**, **1b**, and **1c** (Figure S4a) show several well-resolved resonances at about 7113 (pre-edge peak), 7120, 7126, and 7137 eV. The exact position of these resonances as well as the edge position depends on the oxidation state of the complex; their shifts are quite similar for the three species. A change of the oxidation level from $[LFeCrFeL]^{n+}$ to $[LFeCrFeL]^{(n+1)+}$ results in a shift of approximately +0.8 eV of the edge position. The electronic structure of the iron ions in **1b** can be interpreted as the average of the electronic structures of the iron ions in **1a** and **1c**. In contrast, the edge position of the Cr K-edge (average 5989.14(5) eV) is affected much less by the changes of the oxidation level within the series **1a**−**c**. Only the intensities of the resonances exhibit a marked dependence (Figure S4a). Although the rising edges and the edge positions of **1a** and **1b** are quite similar, the intensities of the resonances at 5993 and at 6002 eV in Figure S4a differ in such a way that **1b** has the lowest intensity at 5993 and the highest intensity at 6002 eV. In contrast to the Fe K-edge measurements on the terminal iron centers, the spectra on the Cr K-edge show no change in the local oxidation state, but small differences in the electronic structure. Irrespective of the overall oxidation level in the $[LFeCrFeL]^{n+}$ series, the Cr oxidation state is invariably +3.

Normalized Fe K-edge XAS spectra of **2b,c** (Figure S4b) show several well-resolved resonances at 7112 (pre-edge peak), 7121, 7128, and 7138 eV. A change of the complex oxidation level by one unit results in a shift of the edge position of about +0.7 eV. The relative peak positions and peak intensities are quite similar for the two samples. In contrast, the edge position of the Co K-edge XANES is only slightly affected by the change of the oxidation level of these complexes; only a shift of ∼0.35 eV is detected. Due to slight differences in the shape of the absorption edges and in the intensities at 7712 eV, the shift of the maximum of the first derivative is misleading (Figure S4b). We conclude that the oxidation state of the Co ions in **2b** and **2c** is +3.

Although the Fe K-edge XANES of **3b,c** cannot be used for an exact analysis, it is noted that the averaged edge position

(65) Ballester, J.; Parker, O. J.; Breneman, G. L. *Acta Crystallogr., Sect. C* **1994**, *50*, 712.
(66) Merlino, S.; Sartori, F. *Acta Crystallogr., Sect. B* **1972**, *28*, 972.
(67) Vincents, H.; Schousboe, F.; Hazell, R. G. *Acta Chem. Scand.* **1972**, *26*, 1375.
(68) Raston, L.; White, A. H. *Aust. J. Chem.* **1977**, *30*, 209.
(69) Mitsumi, M.; Okawa, H.; Sakiyama, G.; Ohba, M.; Matsumoto, N.; Kurisaki, T.; Wakita, H. *J. Chem. Soc., Dalton Trans.* **1993**, 2991.
(70) Woon, T. C.; Mackay, M. F.; O'Connor, M. J. *Inorg. Chim. Acta* **1982**, *58*, 5.
(71) Heeg, M. J.; Blinn, E. L.; Deutsch, E. *Inorg. Chem.* **1985**, *24*, 1118.
(72) Suades, J.; Solans, X.; Font-Albada, M.; Aguilo, M. *Inorg. Chim. Acta* **1985**, *99*, 1.
(73) Marsh, R. E.; Heeg, M. J.; Deutsch, E. *Inorg. Chem.* **1986**, *25*, 118.
(74) (a) Küppers, H.-J.; Neves, A.; Pomp, C.; Ventur, D.; Wieghardt, K.; Nuber, B.; Weiss, J. *Inorg. Chem.* **1986**, *25*, 2400. (b) Konno, T.; Nakamura, K.; Okamoto, K.-I.; Hikada, J. *Bull. Chem. Soc. Jpn.* **1993**, *66*, 2582.
(75) Zabinsky, S. I.; Rehr, J. J.; Ankudinov, A.; Albers, R. C.; Eller, M. J. *Phys. Rev. B*, in press.
(76) Shadle, E. S.; Hedman, B.; Hodgson, K. O.; Solomon, E. I. *Inorg. Chem.* **1994**, *33*, 4235−4244.
(77) Shadle, S. E.; Hedman, B.; Hodgson, K. O.; Solomon, E. I. *J. Am. Chem. Soc.* **1995**, *117*, 2259−2272.
(78) Westre, T. E.; Kennepohl, P.; DeWitt, J. G.; Hedman, B.; Hodgson, K. O.; Solomon, E. I. *J. Am. Chem. Soc.* **1997**, *119*, 6297.

Table 4. Spin Hamiltonian Data Derived from EPR and Magnetic Measurements

	EPR			magnetic measurements									
complex[a]	S_t	g value[b]	$\|D\|$,[c] cm^{-1}	S_1	S_2	S_3	J_a, cm^{-1}	J_t, cm^{-1}	$g_{1,3}$	g_2	$\|D_i\|$,[c] m^{-1}	χ_{TIP}, 10^{-6} cm^3 mol^{-1}	pi,[d] %
1a $[LFe^{II}Cr^{III}Fe^{II}L]^{1+}$	3/2	1.976; 1.973	1.0	0	3/2	0	*e*			1.97	1.0 (Cr)	530	2 (2)
1b $[LFe^{III}Cr^{III}Fe^{II}L]^{2+}$	2			1/2	3/2	0	+26		2.00	1.80	2.0 (Cr)	214	0
1c $[LFe^{III}Cr^{III}Fe^{III}L]^{3+}$	1/2	2.049; 1.869		1/2	3/2	12	−130	−50	2.04	1.98		700	0
2b $[LFe^{III}Co^{III}Fe^{II}L]^{2+}$	1/2	1.963; 2.178		1/2	0	0	*e*		$g_{S_t=1/2} = 2.20$			650	0
2c $[LFe^{III}Co^{III}Fe^{III}L]^{3+}$	1			1/2	0	1/2		+41.5	2.07		1.5 (S_t)	870	0
3b $[LFe^{III}Fe^{II}Fe^{III}L]^{2+}$	1	2.070; 1.930	0.218	1/2	0	1/2	*e*		$g_{S_t=1} = 2.02$		<0.3 (S_t)	550	0
3c $[LFe^{III}Fe^{III}Fe^{III}L]^{3+}$	1/2	1.872; 2.285		1/2	1/2	1/2	*e*		$g_{S_t=1/2} = 2.17$			610	1 (5/2)

[a] The assigned oxidation states are formal ones—for electron book-keeping purposes only. [b] The first number gives $g_{||}$ and the second $g_\perp$. For systems $S_t > 1/2$ these Zeeman g values were obtained from a full-matrix diagonalization of the respective spin Hamiltonian (see the text). [c] The zero-field splitting parameter was obtained from either simulations of the EPR spectra or variable-temperature variable-field magnetization measurements. [d] Paramagnetic impurity of the same molecular mass with the assumed spin state in parentheses. [e] Only the respective spin ground state is populated even at room temperature.

and the positions of the resonances above the edge are shifted by 0.35 eV to higher energy (Figure S4c) in going from **3b** to **3c**.

UV−Vis/Near-IR/IR Spectroscopy. The absorption spectra of complexes were measured in the spectral range 48 000 cm^{-1} (UV) to 400 cm^{-1} (far-IR). The spectra are shown in Figure S5, and Table S18 summarizes the data. In the UV−Vis/near-IR region (210−1100 nm) the spectra consist of very intense transitions which we assign to charge-transfer (CT) transitions due to their large molar extinction coefficients ($\epsilon > 10^3$ M^{-1} cm^{-1}). Interestingly, the mixed valent complexes **1b**, **2b**, and **3b** show electronic transitions at >1100 nm (<9090 cm^{-1}). **1b** displays this transition in the IR at 3400 cm^{-1} (Figure S5a). The broadness (full width at half-maximum, fwhm = 1400 cm^{-1}) and its temperature dependence point to an electronic transition. The intensity of the transition increases with increasing temperature. Complex **3b** has a similar transition at 5550 cm^{-1} (1800 nm) with a fwhm = 1500 cm^{-1}. Again, the intensity of the transition increases with increasing temperature. In **2b** a very broad absorption maximum at 6100 cm^{-1} (1640 nm) with a fwhm = 3200 cm^{-1} (values from a fit with Gaussian line shape) at room temperature is observed (Figure S5).

Since these electronic transitions are not observed in the spectra of **1a**, **1c**, **2c**, and **3c**, we feel that they are intervalence bands of the $Fe^{II}Fe^{III}$ mixed valent part in **1b**, **2b**, and **3b**.

EPR Spectroscopy. The X-band EPR spectra of frozen CH_3CN solutions of **1c**, **2b**, and **3c** at low temperatures consist of axial $S_t = 1/2$ signals. The g values obtained from simulations are given in Table 4.

The S-, X-, and Q-band EPR spectra of a frozen solution of **1a** in CH_3CN show an axial $S_t = 3/2$ signal (Figure S6). The field dependence of the resonances on going from S-, to X-, and to Q-band frequencies indicates that the zero-field splitting is on the order of the microwave energy used (S-band, ~0.1 cm^{-1}; X-band, ~0.3 cm^{-1}; Q-band, ~1.0 cm^{-1}). Therefore, we simulated the spectra with an $S = 3/2$ spin Hamiltonian including an electron Zeeman term and zero-field splitting by full matrix diagonalization. The *effective* values of $g_{||}$ decrease with increasing microwave energy. The *effective* $g_{||}$ of the S-band spectra gives a good estimate for the *Zeeman g* values because in the S-band the limit of strong zero-field splitting is approached. At the Q-band the two terms, Zeeman and zero-field splitting, are nearly of the same order of magnitude, and therefore, these spectra are most sensitive for D. Excellent simulations of all three spectra were obtained with the following parameters: $g_\perp = 1.973$, $g_{||} = 1.976$, and $|D| = 1.0 \pm 0.1$ cm^{-1}.

The EPR spectra of **1b** and **2c** at low temperatures (S-, X-, and Q-band normal mode, X-band parallel mode measured on frozen solutions and powders) consist of a number of relative weak intensities in a wide field range, respectively, which is typical for complexes with an integer spin ground state. Spectra measured on solutions and on powders differ as do spectra measured on powders from preparations with differing precipitation conditions (slow or fast). We made no attempt to simulate these spectra.

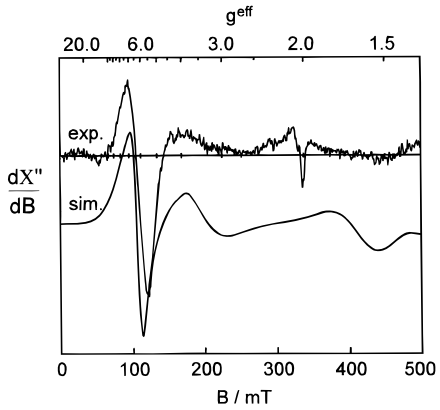

Figure 2. X-band EPR spectrum of a solid sample of **3b** at 10 K (experimental conditions: $\nu = 9.4354$ GHz, $P = 40$ mW, MA = 31 G). Simulation with Gaussian line shapes ($\Gamma = (80, 80, 11)$ mT) and other parameters as given in Table 4.

The X-band EPR spectrum of **3b** (Figure 2) consists of a strong resonance at ~100 mT and two weak resonances at higher field (~200 mT and ~420 mT), indicating a small zero-field splitting. The simulation with an $S = 1$ spin Hamiltonian by full-matrix diagonalization leads to $g_x = g_y = 2.07$, $g_z = 2.02$, and $|D| = 0.22$ cm^{-1}. The main components of the transitions in the three principal directions x, y, and z are visualized in Figure S7. It is important to note that we do not observe a distribution of D in **3b** and that the spin Hamiltonian parameters are consistent with the magnetic measurements and the Mössbauer spectra with applied field (see below).

Magnetic Measurements. Variable-temperature magnetic susceptibilities of solid samples of complexes were measured in the range 2−300 K (for **1c** in the range 2−370 K) by using a SQUID magnetometer and an applied magnetic field of 1.0 T; the results are given in Table 4. The effective magnetic moments, μ_{eff}, of complexes **1a**−**c** as a function of temperature are shown in Figure 3, and those of **2b,c** and **3b,c** in Figure 4. For complexes having an $S_t > 1/2$ ground state, variable-temperature, variable-field magnetization measurements were recorded at 1, 4, and 7 T with temperature variations in the range 2−300 K.

We have employed the following fitting procedure for the

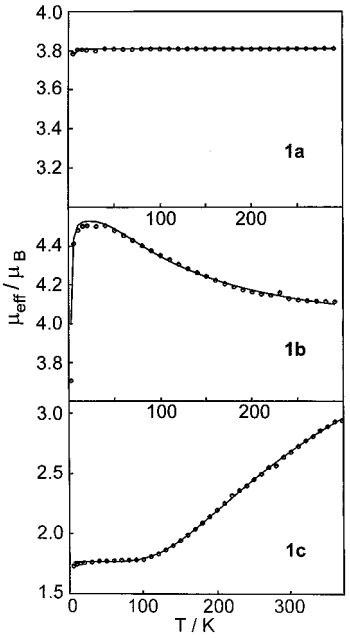

Figure 3. Temperature dependence of the magnetic moments of **1a**−**c**.The fits (solid lines) were obtained using parameters given in Table 4.

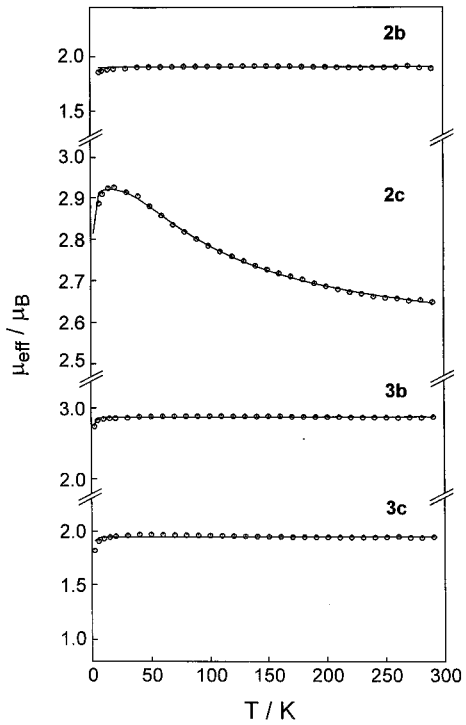

Figure 4. Temperature dependence of the magnetic moments of **2b**,**c** and of **3b**,**c**. Fits (solid lines) were obtained using parameters in Table 4.

$\chi_M T$ data of the variable-temperature measurements and for the χ_M data of the variable-field, variable-temperature magnetization measurements. The spin Hamiltonian used is given in eq 2. It includes the usual isotropic Heisenberg−Dirac−van Vleck (HDvV) exchange Hamiltonian for a trinuclear system, intrinsic zero-field splitting terms, and the local electronic Zeeman terms.[79] A term accounting for a paramagnetic impurity of spin S ($g = 2.00$, same molecular mass) and the contribution of a temperature-independent paramagnetism (TIP) were included. Taking into account a rhombic term $E = 0$ does not give better fits for any complex which is in agreement with the 3-fold symmetry of the complexes.

Since χ_{TIP} is a fit parameter, there is some scatter of these values (530−870) $\times$ 10^{-6} cm^3 mol^{-1}, but the exceptionally small value for **1b** (214 $\times$ 10^{-6} cm^3 mol^{-1}) may indicate that eq 2 does not represent the best model (vide infra). Possible ambiguities of the results were excluded by systematic searches of the fit parameter space including χ_{TIP}. The sign and the magnitude of the J_t value are not straightforwardly derived. There are cases where it is impossible to obtain J_t values from bulk susceptibility measurements.[79,80] To obtain reasonable, physically meaningful values of J_t, we have calculated fit-error contour maps for J_t vs J_a, J_t vs χ_{TIP}, and J_a vs χ_{TIP}. Covariances of parameters and distinctions between local and absolute minima were checked by inspection of these calculations.

Complex **1a** exhibits a temperature-independent effective magnetic moment of 3.81 μ_B in the temperature range 50−300 K indicative of a $S_t = 3/2$ ground state and the absence of thermally populated excited states. An interesting feature is detected in the magnetization data (Figure S8). At a field of 1.0 T the measured magnetization is higher than that calculated by using a simple Brillouin function which is not the case at 4.0 and 7.0 T. This effect is due to a small *intermolecular ferromagnetic interaction* between the $[LFeCrFeL]^{1+}$ cations in the solid state. In complexes **1c**, **2b**, and **3c**, each having an $S_t = {}^1/_2$ ground state, we observe a decrease of μ_{eff} at very low temperatures which is only attributable to an *intermolecular antiferromagnetic interaction*. We do not know the origin of these very weak interactions. The intermolecular ferromagnetic contributions in **1a** compete with the zero-field splitting effects. It is therefore not possible to derive a reliable value for D from the magnetization measurements.

Given that the chromium ion is in the +3 oxidation state, the magnetic measurements yield an oxidation state distribution in **1a** as $[Fe^{II}(ls)Cr^{III}Fe^{II}(ls)]^{1+}$. $Fe^{II}(ls)$ (d^6, t_{2g}^6) is diamagnetic ($S = 0$); the temperature-independent $S_t = {}^3/_2$ state of **1a** corresponds to the d^3 electronic configuration of a central Cr^{III} ion.

The effective magnetic moment of the two-electron oxidized trication of **1a**, namely **1c**, shows a plateau in the temperature range 5−100 K at 1.70 μ_B corresponding to an $S_t = {}^1/_2$ ground state. At temperatures >100 K the magnetic moment increases and reaches 2.94 μ_B at 370 K.

In the following analysis we assume localized oxidation states in **1c** as $[Fe^{III}(ls)Cr^{III}Fe^{III}(ls)]^{3+}$ ($S_1 = S_3 = {}^1/_2$, $S_2 = {}^3/_2$). To reduce the number of parameters for the simulation of this three-spin system, we take advantage of the measured EPR spectra of **1c** which yield $g_{S_t=1/2} = 1.93$ for the ground-state spin $S_t = {}^1/_2$. In the given spin system there exists only one system spin $S_t = {}^1/_2$, which is $|1/2,1\rangle$, where we use the nomenclature $|S_t, S^*\rangle$; S^* is the subspin in Kambe's notation.[81] For this ground state the spin projection formula is given in eq 5.[23]

$$g_{S_t=1/2} = -\frac{1}{3}g_1 + \frac{5}{3}g_2 - \frac{1}{3}g_3 \qquad (5)$$

Here, g_2 represents the local g value of the Cr^{III} ion in **1c**. This value is not expected to change significantly on going from

(79) Simulation program JULIUS written by C. Krebs, F. Birkelbach, and V. Staemmler, unpublished.

(80) (a) Girerd, J.-J.; Papaefthymiou, G. C.; Watson, A. D.; Gamp, E.; Hagen, K. S.; Edelstein, N.; Frankel, R. B.; Holm, R. H. *J. Am. Chem. Soc.* **1984**, *106*, 5491. (b) Dean, N. S.; Mokry, L. M.; Bond, M. R.; O'Connor, C. J.; Carrano, C. J. *Inorg. Chem.* **1996**, *35*, 3541.

(81) Kambe, K. *J. Phys. Soc., Jpn.* **1950**, *5*, 48.

1c to **1a** because for **1a** this Cr^{III} is the only paramagnetic ion present and the experimental EPR spectrum of **1a** immediately yields g_2. Substituting the experimental value $g_2 = 1.97$ from **1a** into eq 5, we obtain the local g value for the Fe^{III}(ls) ion in **1c** as $g_1 = g_3 = 2.04$. In the subsequent simulation and fitting procedure the fixed local g values of 1.97 for Cr^{III} and 2.04 for Fe^{III}(ls) were used. The resulting fit of the data shown in Figure 3 with parameters $J_a = -130$ cm^{-1} and $J_t = -50$ cm^{-1} is excellent. How well is the surprisingly large value of J_t defined? Figure S9a gives the four possible spin states of the system as a function of J_a and J_t (derived from Kambe's treatment[81]). Clearly, the only spin state depending on the value for the terminal coupling J_t is the $|3/2, 0\rangle$ state. The calculated spin ladder and the resulting Boltzmann factors of the spin states at 350 K are shown in Figure S9b. The relevant $|3/2, 0\rangle$ spin state has a population of 13% at this temperature. Thus, we feel that the value of J_t is well defined and physically meaningful. Figure S9c shows an error contour line diagram over the J_a vs J_t area. The covariance of the two coupling constants is striking. Simulations with values at the border of the contour line with the smallest error given in Figure S9c do not reproduce the experimental data as well as the values given above. We estimate an error of ± 5 cm^{-1} for J_t and ± 20 cm^{-1} for J_a.

From the above analysis it is clear that coupling between the two terminal ls Fe^{III} centers is antiferromagnetic in nature and that it is strong. The $S_t = {}^1/_2$ ground state in **1c** is thus attained by intramolecular antiferromagnetic coupling between two terminal ls Fe^{III} ions ($S_{1,3} = {}^1/_2$) and a central Cr^{III} ion ($S_2 = {}^3/_2$).

The effective magnetic moment of the dication **1b** increases from 4.11 μ_B at room temperature to a maximum of 4.51 μ_B at 20 K and then decreases to 3.69 μ_B at 2 K (Figure 3), indicative of a *parallel spin coupling* yielding an $S_t = 2$ spin ground state.

Since the XANES results have shown that in the series **1a**−**c** the oxidation state of the central Cr^{III} is invariant, it appeared to be natural to invoke an oxidation state distribution of $[Fe^{III}(ls)Cr^{III}Fe^{II}(ls)]^{2+}$ in **1b**. In a localized description this would require that the observed $S_t = 2$ ground state is achieved by an intramolecular *ferromagnetic* coupling between a Cr^{III} ion ($S = {}^3/_2$) and one *adjacent* ls Fe^{III} ion ($S = {}^1/_2$). A reasonable fit of the data of **1b** using the spin Hamiltonian eq 2 is possible with the following parameters: $S_1 = {}^1/_2$, $S_2 = {}^3/_2$; $J_a = +26$ cm^{-1}, $g_1 = 2.00$ (fixed), $g_2 = 1.80$ (fitted), $D_2 = 2.0$ cm^{-1}, and $\chi_{TIP} = 214 \times 10^{-6}$ cm^3 mol^{-1}.

There are three indications that this model is not satisfactory: (i) the g value for the Cr^{III} is too small and (ii) the value for χ_{TIP} is unreasonably small for this class of complexes (see Table 4), and, most importantly, (iii) it is hard to reconcile the change of sign of J_a which is *positive* in **1b** and *negative* in **1c** considering that both the ls Fe^{III} ion and the adjacent Cr^{III} ion are in an identical structural environment. Furthermore, the spin Hamiltonian eq 2 must be incomplete since the ground state is still degenerate due to the fact that two resonance structures for **1b** of equal weight exist: $[Fe^{III}(ls)Cr^{III}Fe^{II}(ls)]^{2+}$ and $[Fe^{II}(ls)Cr^{III}Fe^{III}(ls)]^{2+}$. *This represents the classic situation where double exchange contributions cannot be neglected.*

The dication **2b** exhibits a nearly temperature-independent effective magnetic moment of 1.90 ± 0.1 μ_B in the range 30−300 K (Figure 4). Below 30 K, μ_{eff} decreases slightly, which is indicative of a small intermolecular antiferromagnetic coupling which was modeled by taking into account a Curie−Weiss constant Θ of -1.3 K. This behavior is in accord with an oxidation state distribution of $[Fe^{III}(ls)Co^{III}(ls)Fe^{II}(ls)]^{2+}$ containing a single paramagnetic low-spin Fe^{III} ion.

The trication in **2c** displays a μ_{eff} of 2.65 μ_B at 295 K which increases to a value of 2.92 μ_B at 20 K and then decreases to 2.48 μ_B at 2 K. This behavior is typical for two ferromagnetically coupled $S_i = {}^1/_2$ spins, yielding an $S_t = 1$ ground state (Figure 4); the simulation gives $J_t = +41.5$ cm^{-1} and $g_1 = g_3 = 2.07$. The magnetization data confirm the $S_t = 1$ spin ground state (Figure S10). With the values of J_t and $g_1 = g_3$, fixed as given above, a zero-field splitting parameter $|D| = 1.5$ cm^{-1} was obtained.

The trication **3c** exhibits a nearly temperature-independent effective magnetic moment of 1.95 ± 0.1 μ_B (Figure 4). The simulation with an effective $S_t = {}^1/_2$ spin yields $g = 2.17$, which corresponds nicely with the isotropic g value of the EPR spectrum. The observed ground state originates then from antiferromagnetic coupling of three local $S_i = 1/2$ spin states $[Fe^{III}(ls)Fe^{III}(ls)Fe^{III}(ls)]^{3+}$. The coupling constant between adjacent metal centers J_a is <-400 cm^{-1} and independent of J_t. For this spin system there are three system spin states, namely $|{}^1/_2, 1\rangle$, $|{}^1/_2, 0\rangle$, and $|{}^3/_2, 1\rangle$. If $|J_a| > |J_t|$ holds, then the ground state is $|{}^1/_2, 1\rangle$. The only spin state of which the energy depends on J_t is $|{}^1/_2, 0\rangle$, which is also a doublet. Only the energy of the nondegenerate state $|{}^3/_2, 1\rangle$ depends on J_a, and consequently, only the reduction of the energy of this state leads to an increase of μ_{eff} at higher temperatures.

The dication **3b** possesses a temperature-independent effective magnetic moment of 2.88 μ_B indicative of an $S_t = 1$ spin ground state and no thermally accessible excited spin states (Figure 4). No zero-field splitting effects of the $S_t = 1$ spin state are detectable. This is also manifestated by the magnetization measurements (Figure S10). Simulations of the magnetization measurements with an effective $S_t = 1$ spin Hamiltonian indicate an upper limit for $|D|$ of 0.3 cm^{-1}.

Mössbauer Spectroscopy. All compounds have been extensively studied by Mössbauer spectroscopy in zero and applied magnetic fields. The zero-field Mössbauer spectra were measured temperature-dependent from 4.2 K to room temperature, and the spectra with applied field were measured field- and temperature-dependent. In general, the spin ground states are well separated from the excited spin states, and the limit of strong coupling ($J \gg D$) is valid. Therefore, we have used an effective spin Hamiltonian for the description of the respective spin ground states resulting from the spin coupling of the local spins, eq 3. In zero applied field nearly all samples displayed pure quadrupole spectra—even at 4.2 K. The magnetically perturbed spectra of paramagnetic species at $B \geq 1$ T were simulated in the slow relaxation limit. Thus, the observed field dependence of the relaxation rate due to spin−spin interactions in the solid state is broken. The zero-field spectra of the complexes were readily simulated, and the data are summarized in Table 5.

The sign of the quadrupole splitting parameter, ΔE_Q, was unambiguously determined from the spectra measured in an applied magnetic field. The data in Table 5 contain the values of the 4.2 K spectra only. Unless stated otherwise the spectra show a small temperature dependence of the isomer shift due to a second-order Doppler effect. Also, the quadrupole splitting was found to exhibit no significant temperature dependence even for the central ls Fe^{III} ion in **3c** with quasi-O_h symmetry. This observation indicates that the orbital degeneracy of the T ground states is significantly lifted by the trigonal ligand field.

The spectra of **1a**, **1c**, and **2c** consist of a single quadrupole doublet. The spectrum of **1b** also displays only a single quadrupole doublet when microcrystalline, rapidly precipitated samples are used. More slowly grown, i.e., more visibly crystalline, samples show a broadening of this doublet and, in addition, new weak spectral features (Figure S11). This effect

Table 5. Mössbauer Data of $[LFeMFeL]^{n+}$ with and without an Applied Magnetic Field[a]

		δ, mm s^{-1}	ΔE_Q, mm s^{-1}	rel area, %	$\bar{\bar{A}}/\mu_N g_N$, T	$a^{iso}/\mu_N g_N$, T	$\bar{\bar{g}}$	g^{iso}	D, cm^{-1}
1a $[LFeCrFeL]^{1+}$		0.54	−0.14	100	0.65; 0.65; 0.62	0.64	1.976; 1.973; 1.973	1.974	1.0
1b $[LFeCrFeL]^{2+}$		0.42	+1.11	100	−0.86; −0.86; −2.75	$A^{iso} = -1.49$	2.0; 2.0; 2.0	2.0	0.59
1c $[LFeCrFeL]^{3+}$		0.34	+2.00	100	4.26; 4.26; 0.52	−9.05	1.869; 1.869; 2.049	1.929	
2b $[LFeCoFeL]^{2+}$	Fe^{III}	0.32	+1.68	50	−16.12; −16.12; 3.92	−9.49	2.178; 2.178; 1.963	2.106	
	Fe^{II}	0.44	−0.22	50	0.69; 0.69; 0.89	0.76	2.178; 2.178; 1.963	2.106	
2c $[LFeCoFeL]^{3+}$		0.31	+1.92	100	−5.84; −5.84; 1.83	−6.57	2.066; 2.066; 2.066	2.066	−1.50
3b $[LFeFeFeL]^{2+}$	N_3S_3	0.39	+1.36	66	−7.65; −7.65; 2.49	$A^{iso} = -4.27$	2.070; 2.070; 1.930	2.02	−0.218
	S6	0.53	+0.87	34	−11.35; −11.35; 2.67	$A^{iso} = -6.68$	2.070; 2.070; 1.930	2.023	−0.218
3c $[LFeFeFeL]^{3+}$	N_3S_3	0.33	+1.85	67	−2.76; −2.76; 2.73	−1.40	2.306; 2.306; 1.859	2.157	
	S6	0.47	+1.76	33	1.97; 1.97; 5.58	−9.52	2.306; 2.306; 1.859	2.157	

[a] The values for the isomer shift δ and the quadrupole splitting ΔE_Q are given for the spectra at $T = 4.2$ K.

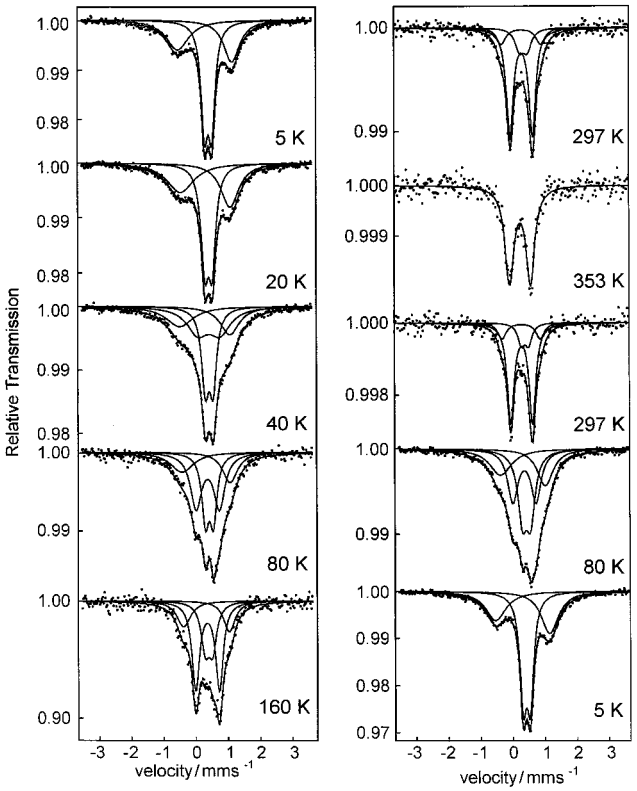

Figure 5. Temperature dependence of the zero-field Mössbauer spectra of **2b** (warming and cooling).

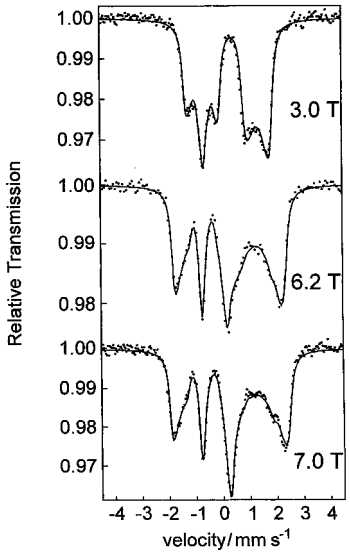

Figure 6. Mössbauer spectra of **1c** at 4.2 K in applied magnetic fields (3.0, 6.2, and 7.0 T perpendicular to the γ-beam).

was traced back to magnetic phenomena in the solid state which influence the electronic relaxation rates. Experimentally this is verified by measuring the Mössbauer spectra of samples of varying crystallinity in weak applied fields (∼40 mT) in the temperature range 1.5−4.2 K. The relaxation is strongly dependent on the size of the crystallites of the sample. We have not studied these effects in greater detail but used microcrystalline powder samples of **1b** instead.

The Mössbauer spectra of the three-iron complexes **3b** and **3c** each exhibit two quadrupole doublets with relative ratios of 2:1. We assign the doublet with $^2/_3$ of the intensity to the two terminal iron centers and the other with $^1/_3$ of the intensity to the single central iron ion.

The dicationic cobalt compound **2b** shows an interesting behavior. In the 4.2 K spectrum two doublets of equal intensity are observed (Figure 5). With increasing temperature a new doublet with nearly the mean values of the isomer shift and the quadrupole splitting appears at the expense of the former two doublets. At 353 K only this doublet is detected. Cooling the sample leads to the reverse behavior.

The Mössbauer spectra recorded at 4.2 K in applied magnetic fields of 2.1, 4.0, 6.2, and 7.0 T of **1a** displayed in Figure S11a show that a small internal magnetic field is measured at the iron sites although they are formally diamagnetic Fe^{II}(ls). From simulations using a spin Hamiltonian for the $S_t = {}^3/_2$ system spin with a fixed g value derived from the EPR spectra and a fixed zero-field splitting of $D = 1$ cm^{-1} in the slow relaxation limit, a hyperfine tensor $\bar{\bar{A}}/\mu_N g_N = (+0.65; +0.65; +0.62)$ T was obtained. The simulations are not very sensitive with respect to the sign of the quadrupole splitting. Nevertheless, the spectra measured in small applied fields were best simulated with a negative sign for ΔE_Q.

Excellent simulations in the slow relaxation limit shown in Figure 6 were obtained for **1c**. The sign of the quadrupole splitting is unambiguously positive, and the asymmetry parameter η is zero. The effective hyperfine tensor for the system spin of $S_t = {}^1/_2$ is very anisotropic (Table 5). Spin projection, eq 6, yields the intrinsic hyperfine tensor.

$$\bar{\bar{a}}_{S_1=1/2} = -3\bar{\bar{A}}_{S_t=1/2} \tag{6}$$

The spectra of the dication **1b** with applied field were found to be affected by crystallinity effects of the type described above. In Figure S11 the 7 T spectra at 4.2 K of sample A (microcrystalline) and sample B (larger crystals) are compared. The broadening of the highest energy absorption lines is more pronounced in the spectrum of sample B. These effects have a

profound influence on the A_{zz} parameter, which exhibits a distribution. In contrast, the A_{xx} and A_{yy} parameters are well defined.

The field-dependent spectra of **2b** were measured at low temperatures only. The simulations in the slow relaxation regime with an effective spin Hamiltonian of $S_t = {}^1/_2$ with the g values fixed at the values of the EPR spectrum yield a very anisotropic $\bar{\bar{A}}$ tensor of the Fe^{III} site with a change of the sign on going from A_{zz} to A_{xx} and A_{yy} (Table 5 and Figure S12). The quadrupole splitting is clearly positive. The simulations of the spectrum recorded at high field (7 T) demonstrate again the presence of an internal field even at the Fe^{II}(ls) site as in **1a**. The sign of the quadrupole splitting of this iron center is not unambiguously determined, but a negative sign appears to be more likely.

A good reproduction of the experimental spectra of **2c** shown in Figure S12a was achieved by simulations with an effective spin Hamiltonian of $S_t = 1$ in the slow relaxation limit. The value of the zero-field splitting was taken from the magnetization data, and the sign is unambiguously determined as negative ($D = -1.5\ cm^{-1}$). The g values were isotropically fixed at the value derived from the magnetization measurement. The quadrupole splitting is positive, and the asymmetry parameter η is zero. The spectra at small and intermediate fields (1 and 4 T) are very sensitive to changes of the value of D. Therefore, the poor quality of these simulations is due to a distribution of D values induced by solid-state effects. The derived hyperfine tensor (Table 5) is again very anisotropic. Spin projection, eq 7, yields

$$\bar{\bar{a}}_{S_1=1/2} = 2\bar{\bar{A}}_{S_t=1} \qquad (7)$$

the intrinsic hyperfine tensor. For the zero-field splitting no spin projection is possible because the local doublet states do not possess a local zero-field splitting. The origin of the zero-field splitting is therefore due to spin dipolar interactions.

The field and temperature dependencies of the Mössbauer spectra of **3b** were perfectly simulated with an effective spin Hamiltonian for the $S_t = 1$ spin ground state in the slow relaxation limit (Figure 7). The spin parameters (g_x, g_y, g_z, D) were successively optimized in conjunction with the simulation of the EPR and magnetic mesurements. The three methods yield one, well-defined parameter set. The sign of the zero-field splitting is unambiguously derived from the Mössbauer spectra. The quadrupole splitting is positive and the asymmetry parameter η is zero for both doublets. No solid-state effects are observable for this complex, consistent with the zero-field Mössbauer and EPR spectra.

To derive the hyperfine tensors of the terminal and central iron ions in **3c**, we measured the field dependence of the Mössbauer spectra at 4.2 K (Figure S13). The simulations were carried out with an effective spin Hamiltonian $S_t = {}^1/_2$. To limit the number of parameters, numerical g values obtained from the powder EPR spectrum were used. The solution is difficult because the two different types of iron centers possess similar parameters, giving rise to a strong overlap. Simulations in the fast and slow relaxation limits yield acceptable reproductions of the experimental data. The simulations are not very sensitive to changes in the components of the hyperfine coupling because the isotropic hyperfine constant is very small. From numerous calculations we arrive at the conclusion that for the high-field spectrum (7 T) the limit of slow relaxation is valid. The 3.5 T spectrum is the most difficult to simulate because it is in the intermediate relaxation regime where a dynamic line width model is appropriate. Figure S13 displays simulations which were obtained in the fast relaxation limit with the parameter set given in Table 5. Some features of the measured spectrum

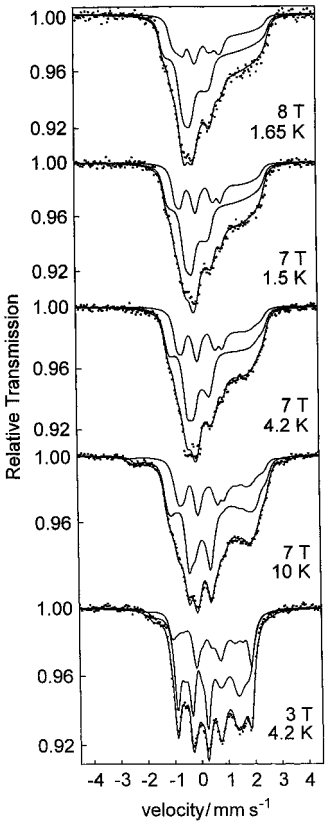

Figure 7. Mössbauer spectra of **3b** in applied magnetic fields (8.0, 7.0, and 3.0 T perpendicular to the γ-beam) at 4.2 and ~1.5 K.

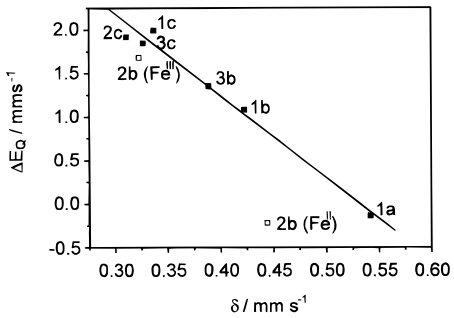

Figure 8. Quadrupole splitting, ΔE_Q, vs the isomer shift, δ, of the terminal iron sites of complexes measured at 4.2 K in applied field.

are better reproduced in the slow relaxation limit and others in the fast relaxation limit.

Inspection of the data given in Table 5 reveals an interesting correlation. A plot of the isomer shift δ versus the quadrupole splitting ΔE_Q for complexes **1a**, **1b**, **1c**, **2c**, **3b**, and **3c** displayed in Figure 8 shows that the two quantities are linearly correlated. Only for **2b** this correlation appears *not* to hold for the ls Fe^{II} site. Although it is well established in Mössbauer spectroscopy that the isomer shift is a measure for the d^n electron configuration (oxidtion state) of the iron ion, the quadrupole splitting ΔE_Q, in general, is not. Values of δ and ΔE_Q for complexes **1c**, **2c**, and **3c** are very similar at $\delta \approx 0.32$ mm s^{-1} and $\Delta E_Q \approx +1.9$ mm s^{-1}. For these complexes the oxidation state assignment of both terminal iron ions is +3, in agreement with all other spectroscopic and magnetochemical data. These ions possess a $(1e)^4(a_1)^1$ electron configuration. On the other hand, **1a** clearly contains two low-spin Fe^{II} ions ($(1e)^4(a_1)^2$). It is therefore gratifying that the mixed valence class III species **1b** displays Mössbauer parameters which are nearly the exact mean values of those of **1a** and **1c**. This allows the straightforward

assignment of a +2.5 oxidation state for both terminal iron ions in **1b**. Similarly, for the class III species **3b** assuming an average oxidation state of +2.67 per iron ion, the above correlation predicts δ and ΔE_Q values of 0.39 and 1.50 mm s^{-1}, respectively, for the two terminal iron ions, in very close agreement with the experimental values of 0.39 and 1.36 mm s^{-1}.

Discussion

As stated above, the idealized symmetry of all trinuclear cationic units is S_6; considering only the metal centers within their first coordination spheres, it is D_{3d}. The terminal iron ions in the *fac*-N_3S_3 coordination sphere belong to C_{3v}, and the central metal ion belongs to D_{3d}. Trigonal distortion of the octahedral coordination polyhedron leads to a splitting of the t_{2g}-orbitals (in O_h) into a doubly degenerate orbital set (1e in C_{3v}) and a nondegenerate orbital (a_1 in C_{3v}) where two directions of this splitting are possible ($a_1$1e or 1e a_1). In a ligand field approach these orbital sets can be expressed as linear combinations of the metal d-orbitals.[82,83] The a_1-orbital corresponds to a d_{z^2} orbital, where the *z* axis coincides with the 3-fold symmetry axis of the trinuclear cations. The e(t_{2g})-orbitals are π-orbitals with respect to the metal−ligand bonds and the e(e_g)-orbitals are of the σ type.[84]

To identify the local magnetic orbitals, it is necessary to know the direction of the trigonal splitting. Experimentally, this information is derived from the Mössbauer spectra. The valence electron contribution to the electric field gradient, $(EFG)_{val}$, was estimated by a simple ligand field consideration: the expectation values for the $(EFG)_{val}$ tensor elements are known for the individual metal d-orbitals.[6,85] In a recent publication we derived these tensor elements for trigonal symmetry.[86] For a d^5 ls system there are two possible electron configurations in trigonal symmetry: $(1e)^4(a_1)^1$ and $(a_1)^2(1e)^3$ leading to $V_{zz} = +4/7\ e\cdot\langle r^{-3}\rangle$ and $V_{zz} = -2/7\ e\cdot\langle r^{-3}\rangle$, respectively. *Therefore, the experimental determination of the sign of the quadrupole splitting by Mössbauer spectroscopy directly yields the respective electron configuration.*

[LFeCrFeL]$^{1+}$ (1a). From the experimentally determined $S_t = {}^3/_2$ ground state and the temperature independence of the effective magnetic moment, it follows that the oxidation state distribution for the monocationic complex **1a** is [Fe^{II}(ls)Cr^{III}-Fe^{II}(ls)]$^{1+}$ where the Fe^{II} ions are in a low-spin d^6 configuration. The small quadrupole splitting, ΔE_Q, proves that the t_{2g} shell is filled, yielding an $^1A_1$ ground state with zero contribution to the EFG from the valence shell. Therefore, the small value of ΔE_Q arises to a first approximation from the ligand contribution to the $(EFG)_L$.

The only unexpected experimental result is the observation of a small internal magnetic field at the diamagnetic Fe^{II}(ls) ions. In a phenomenological description this effect is called a supertransferred hyperfine field which invokes a coupling between a nucleus A and the electrons of a second nucleus B. This contribution is often small and negligible because coupling between the nucleus A and the electrons of A is, in general, much larger. Two mechanisms have been proposed for the origin of this supertransferred hyperfine field.[87,88] The first one is spin polarization which would produce a positive spin density in contrast to the observed negative spin density (positive hyperfine tensor) in **1a**. Therefore, the second mechanism invoking intramolecular dipolar fields is most likely the origin of the measured supertransferred hyperfine field (∼1 T).[88] The marked anisotropy of the **A** tensors in this series of complexes proves the presence of such strong dipolar fields.

Chart 3

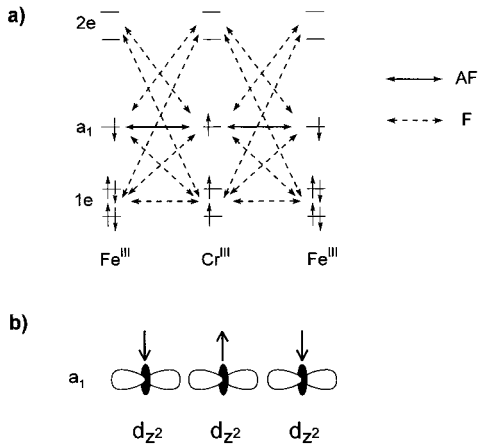

[LFeCrFeL]$^{3+}$ (1c). Complex **1c** also displays only one quadrupole doublet in the Mössbauer spectrum, rendering the two terminal iron ions equivalent. As the oxidation state of the chromium ion remains +3, both iron ions are assigned a +3 oxidation state. The decreasing isomer shift on going from **1a** to **1c** and the increasing quadrupole splitting are consistent with an Fe^{III}(ls) formulation. The d^5 ls electron configuration induces a significant valence electron contribution to the EFG. The sign of the quadrupole splitting is positive, indicating thereby an e(t_{2g})$^4a_1^1$ configuration of the Fe^{III} ions (Chart 3). The observed $S_t = {}^1/_2$ ground state of **1c** originates then from an antiferromagnetic coupling between the adjacent Fe^{III} ($S_1 = S_3 = {}^1/_2$) ions and the Cr^{III} ($S_2 = {}^3/_2$) ion. Note that there is also a strong antiferromagnetic interaction between the terminal iron centers ($J_t = -50$ cm^{-1}). In Chart 3a the possible interaction pathways between adjacent metal centers are displayed and classified as ferro- or antiferromagnetic according to the Goodenough−Kanamori rules.[89−94] All pathways except one are ferromagnetic in nature. The only pathway leading to an antiferromagnetic coupling is the direct interaction of the a_1-orbitals (Chart 3b) which then dominates all other contributions.

[LFeCrFeL]$^{2+}$ (1b). Since the energy of the Cr K-edge of **1b** is nearly identical to that of **1a** and **1c**, the dication in **1b** can be assigned an oxidation state distribution [Fe^{II}(ls)$Cr^{III}Fe^{III}$-(ls)]$^{2+}$ (Chart 4a) using localized oxidation states. In this case the a_1−a_1 exchange pathway between the single ls Fe^{III} ($S_1 = {}^1/_2$) ion and the Cr^{III} ($S_2 = {}^3/_2$) ion would have to yield an $S_t = 1$ ground state. Obviously, this is in sharp contrast to the experimentally observed $S_t = 2$ ground state for **1b**. Therefore, a localized model cannot be valid for **1b**. The observation of a single quadrupole doublet for *both* iron ions in **1b**—even at 4.2

(82) Ballhausen, C. J. *Introduction to Ligand Field Theory*, 1st ed.; McGraw-Hill: New York, 1962; p 68.
(83) Trogler, W. C. *Inorg. Chem.* **1980**, *19*, 697.
(84) Albright, T. A.; Burdett, J. K.; Whangbo, M. H. *Orbital Interactions in Chemistry*; Interscience: New York, 1985; p 381.
(85) Gütlich, P. In *Mössbauer Spectroscopy*; Gonser, U., Ed.; Springer-Verlag: Berlin, Heidelberg, New York, 1975.
(86) Bossek, U.; Nühlen, D.; Bill, E.; Glaser, T.; Wieghardt, K.; Trautwein, A. X. *Inorg. Chem.* **1997**, *36*, 2834.
(87) Evans, B. J.; Swartzendruber, L. J. *Phys. Rev. B* **1972**, *6*, 223.
(88) Vandenberghe, R. E.; Grave, E. D. In *Mössbauer Spectroscopy Applied to Inorganic Chemistry*, *Vol. 3*; Long, G. J., Grandjean, F., Eds.; Plenum Press: New York, 1989; p 101.
(89) Goodenough, J. B. *Phys. Rev.* **1955**, *79*, 564.
(90) Goodenough, J. B. *J. Phys. Chem. Solids* **1958**, *6*, 287.
(91) Goodenough, J. B. *Magnetism and the Chemical Bond*; Interscience: New York, 1963.
(92) Kanamori, J. *J. Phys. Chem. Solids* **1959**, *10*, 87.
(93) Anderson, P. W. *Phys. Rev.* **1959**, *115*, 2.
(94) Anderson, P. W. In *Magnetism*; Rado, G. T., Suhl, H., Eds.; Academic Press: New York, 1963.

Chart 4

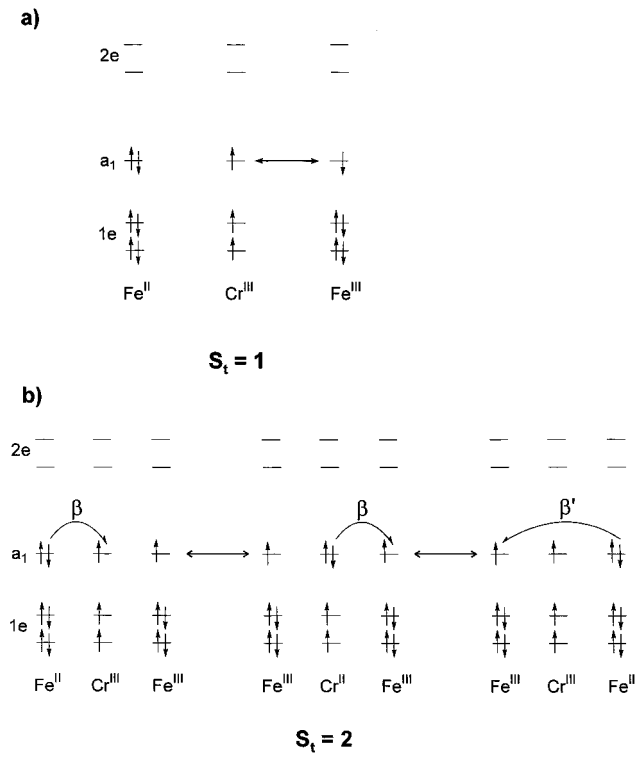

K—requires a formal oxidation state of +2.5 for both iron ions. Furthermore, Hush's line width criterion[95] ($\Delta\nu_{1/2} = (2310\nu_{max})^{1/2}$) applied to the intervalence transition at 3400 cm^{-1} allows the assignment of **1b** to class III (fully delocalized) rather than class II according to Robin and Day.[96]

In the frame of valence bond theory the ground state of **1b** can be described by several nearly degenerate electronic configurations (resonance structures, canonical forms).[97] The three relevant resonance structures for **1b** shown in Chart 4b are formally interrelated by one-electron-transfer steps. Since electron delocalization originates from electrostatic interactions which do not operate on the spin part of the wave function, this electron transfer must occur without spin flip.[5] Electron transfer takes place within the a_1 orbitals. Resonance structures invoking the a_1 orbitals at Fe and the 2e orbitals at Cr are not considered to play a role because according to group theoretical considerations the electron-transfer integral β is zero due to symmetry constraints. Thus, rationalization of the $S_t = 2$ ground state of **1b** is effectively achieved by invoking a double exchange mechanism *over three metal sites.*

At this point it is appropriate to compare these findings with those reported for the extensively studied class III complex $[\{(tmcn)Fe^{2.5}\}_2(\mu\text{-}OH)_3]^{2+}$ with an $S_t = {}^9/_2$ ground state[101−104] for

Chart 5

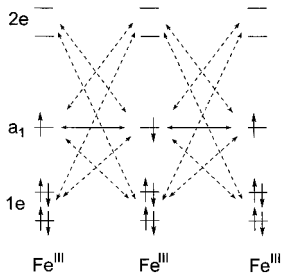

which the double exchange mechanism has been described. Stabilization of the $S_t = 2$ ground state in **1b** of ∼100 cm^{-1} is found to be smaller than that of the $S_t = {}^9/_2$ ground state (∼700 cm^{-1}) in the dinuclear species. This fact can be rationalized as follows: (i) The three resonance structures shown in Chart 4b for **1b** do not contribute with the same weight. The structure invoking a central Cr^{II} is energetically more unfavorable than the other two because it is more difficult to reduce Cr^{III} to Cr^{II} than Fe^{III} to Fe^{II}. On the other hand, the shapes of the Cr K-edge peaks of **1a**−**c** do suggest that the central Cr ion in **1b** possesses at least some Cr^{II} character in contrast to **1a** and **1c**. (ii) The transfer integral β' for the terminal Fe sites in **1b** is smaller than the corresponding integral β for adjacent Fe ions in $[(tmcn)_2Fe_2(\mu\text{-}OH)_3]^{2+}$ simply due to the fact that the Fe···Fe distance is ∼6 Å in **1b** and ∼2.5 Å in the latter complex.

$[LFeFeFeL]^{3+}$ (3c). From the Mössbauer data plotted in Figure 8 it clearly follows that both terminal iron ions in **3c** must be assigned an oxidation state of +3, which yields a central low-spin ferric ion. Interestingly, the Mössbauer parameters reported for $[(aet)_3Co^{III}Fe^{III}Co^{III}(aet)_3]^{3+}$ ($S_t = {}^1/_2$), which contains a central ls $Fe^{III}S_6$ moiety in a diamagnetic ligand matrix (δ = 0.40 mm s^{-1}, $|\Delta E_Q|$ = 1.70 mm s^{-1} at 104 K[105]), are very similar to those reported here for **3c** at 4 K. Thus, **3c** is a $[Fe^{III}(ls)Fe^{III}(ls)Fe^{III}(ls)]^{3+}$ species as shown in Chart 5. The differing signs of the effective hyperfine couplings constants ($A^{iso}_{1,3} = -0.93g_N\mu_N T$, $A^{iso}_2 = +3.17g_N\mu_N T$) demonstrate that the local spins of the terminal iron ions are aligned parallel to the system spin and the local spin of the central iron ion is aligned antiparallel to the system spin, which gives rise to the $|{}^1/_2,1\rangle$ ground state. All exchange pathways except the a_1−a_1 interaction are of ferromagnetic nature. Therefore, the observed very strong antiferromagnetic coupling ($J_a < -400$ cm^{-1}) originates from the direct exchange between local a_1-orbitals. The energy difference between the local magnetic orbitals in this homotrinuclear complex is smaller than in the heterotrinuclear complex **1c**, which yields a larger energy splitting, resulting in a stronger antiferromagnetic coupling. Delocalization of electron density in the bonding region results in the observed reduction of the intrinsic hyperfine coupling constant. We describe this interaction as *the onset of metal−metal bonding.*

$[LFeFeFeL]^{2+}$ (3b). The one-electron reduction of **3c** yielding **3b** leads to a reduction of the formal oxidation state of the two terminal iron ions *and* the central iron ion. From Figure 8 the assignment of a formal oxidation state for the terminal iron centers as +2.67 is appropriate. Simple charge considerations imply then the same oxidation state for the central iron ion. This situation can be described by three resonance structures

(95) Hush, N. S. *Prog. Inorg. Chem.* **1967**, *8*, 357, 391.
(96) Robin, M. B.; Day, P. *Adv. Inorg. Chem. Radiochem.* **1967**, *10*, 247.
(97) March, J. *Advanced Organic Chemsitry*, 4th ed.; John Wiley & Sons: New York, 1992; pp 26−36.
(98) Girerd, J.-J.; Papaefthymiou, V.; Surerus, K. K.; Münck, E. *Pure Appl. Chem.* **1989**, *61*, 805.
(99) Blondin, G.; Girerd, J.-J. *Chem. Rev.* **1990**, *90*, 1359.
(100) Blondin, G.; Borshch, S.; Girerd, J.-J. *Comments Inorg. Chem.* **1992**, *12*, 315.
(101) Drüke, S.; Chaudhuri, P.; Pohl, K.; Wieghardt, K.; X.-Q., D.; Bill, E.; Trautwein, A. X.; Winkler, H.; Gurman, S. J. *J. Chem. Soc., Chem. Commun.* **1989**, 59.
(102) Ding, X.-Q.; Bominaar, E. L.; Bill, E.; Winkler, H.; Trautwein, A. X.; Drüeke, S.; Chaudhuri, P.; Wieghardt, K. *J. Chem. Phys.* **1990**, *92*, 178.
(103) Gamelin, D. R.; Bominaar, E. L.; Kirk, M. L.; Wieghardt, K.; Solomon, E. I. *J. Am. Chem. Soc.* **1996**, *118*, 8085.
(104) Kahn, O. *Molecular Magnetism*, 1st ed.; VCH Publisher: New York, 1993.
(105) Freeh, G.; Chapman, K.; Blinn, E. *Inorg. Nucl. Chem. Lett.* **1973**, *9*, 91.

Chart 6

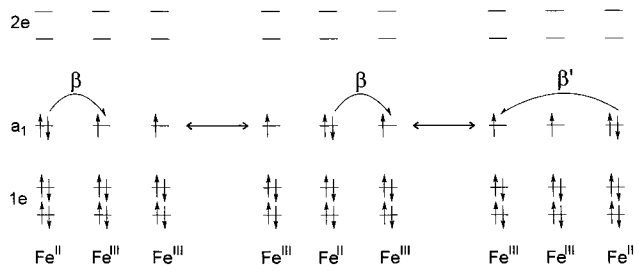

(Chart 6), each of which consists of one Fe^{II} center and two Fe^{III} centers. The positive sign of the quadrupole splitting indicates that the local a_1-orbitals are the magnetic orbitals. The near energetic degeneracy of these resonance structures implies an equivalent contribution of these to the resonance-stabilized (delocalized) ground state. The above delocalized description is supported by a low-energy electronic transition at 5500 cm^{-1}. The observed independence of this absorption maximum and of its extinction coefficient on varying the solvent from acetonitrile to acetone and dichloromethane corroborates the assignment of **3b** as a class III mixed valent compound where the excess electron is quantum-mechanically delocalized over three metal centers.

The origin of the $S_t = 1$ ground state which is the only populated state up to room temperature is again readily understood by a double exchange mechanism over three metal centers via the a_1 pathway (Chart 6). Only parallel alignment of the three respective local spins allows the excess electron to be transferred over all *three* metal centers. The negative sign of the effective Mössbauer hyperfine coupling constants A_i^{iso} indicates positive spin density at the terminal and central iron centers, respectively, corroborating thereby the above picture. In a hypothetical $S_t = 0$ ground state, delocalization would be limited to two metal centers.

[LFeCoFeL]$^{3+}$ (2c). The Mössbauer spectra of **2c** unambiguously show that the terminal iron ions are low-spin ferric with an $(1e)^4(a_1)^1$ electron configuration. Thus, **2c** can be described as $[Fe^{III}(ls)Co^{III}(ls)Fe^{III}(ls)]^{3+}$ with localized valencies. Rather surprisingly this species possesses an $S_t = 1$ ground state which implies a *ferromagnetic* coupling between the two $S_1 = S_3 = {}^1/_2$ local spins of the terminal iron centers. (Note that J_t in **1c** is negative, indicating an antiferromagnetic exchange interaction). In accord with the magnetochemistry of **2c**, the sign of the effective Mössbauer hyperfine coupling constant is negative.

It is by no means straightforward to understand the nature of this ferromagnetic interaction in **2c** yielding an $S_t = 1$ rather than a diamagnetic ground state. The Hubbard−Anderson model Hamiltonian[99,106,107] provides a suitable theoretical frame, the details of which we will outline in a subsequent theoretical paper. In essence, we will show the following. The ls d^5 ls d^6 ls d^5 electron configuration represents the ground state for **2c**; it is isoelectronic to one of three resonance structures given for **3b** in Chart 6 where the excess electron is localized on the central iron ion. In the *delocalized* case of **3b** the other two configurations mix in first-order perturbation of electron transfer because they belong to the same energy subspace, yielding a well-separated $S_t = 1$ ground state (double exchange mechanism). In contrast, in the localized case of **2c** the other two possible configurations mix in second-order perturbation because they are energetically highly separated charge-transfer states contributing only very little to the stabilization of the triplet state (superexchange mechanism). It is the advantage of the Hubbard−Anderson model Hamiltonian that it deals with both double exchange and superexchange mechanisms depending only on the level of perturbation.

[LFeCoFeL]$^{2+}$ (2b). The mixed valence species **2b** belongs to class II according to Robin and Day as is clearly deduced from their temperature-dependent Mössbauer spectra which at 4.2 K display two distinct quadrupole doublets, one for a low-spin ferric ion and the other for a low-spin ferrous ion. At room temperature only a single doublet is observed. Thus, on the time scale of a Mössbauer experiment (10^{-7} s) electron hopping is evidenced. In accord with this interpretation an intervalence charge-transfer transition is observed at 6100 cm^{-1}.

The Mössbauer spectra reveal an interesting facet. Despite the fact that electron hopping in **2b** is a dynamic process, no significant line broadening which is usually indicative of coalescence processes is detectable upon raising the temperature. Similar observations have been described previously and have recently been interpreted by Gütlich and Hendrickson.[108] These authors reason that due to solid-state cooperative effects the potential energy surface changes as the temperature increases,[109,110] in which case, electron hopping is possible without coalescence. The presence of the necessary cooperative effects is experimentally borne out by the observed variability of the Mössbauer spectra of **2b** on sample preparations (crystallinity).

Conclusion

In this study we have shown that the mononuclear species $[Fe^{III}L]$ containing a *cis*-N_3S_3 donor set is well suited to form a series of isostructural trinuclear complexes in the presence of other transition metal ions. $[LFeMFeL]^{n+}$ species contain a linear array of two terminal iron ions and a central MS_6 unit (M = Cr, Co, Fe); the structure of the $[N_3FeS_3MS_3FeN_3]^{n+}$ core is in all cases face-sharing octahedral with six μ_2-thiolato bridges. Electrochemically and chemically the charge of these trications can be varied between 1+ and 3+ (4+) without changing the gross overall structure. These isostructural mono-, di-, and trications show remarkable electronic structural features: localized and delocalized formal oxidation state distributions have been encountered. Double exchange and superexchange mechanisms are intimately coupled.

Interpretation of the electronic structure via a superexchange mechanism between localized paramagnetic centers with localized oxidation states has been achieved for **1c** ($[Fe^{III}(ls)Cr^{III}$-$Fe^{III}(ls)]^{3+}$, $S_t = {}^1/_2$). Surprisingly, and more difficult to understand, the ferromagnetic $S_t = 1$ ground state is observed for **2c** with a localized $[Fe^{III}(ls)Co^{III}Fe(ls)]^{3+}$ oxidation state distribution, whereas **3c** has the expected antiferromagnetic $S_t = {}^1/_2$ ground state ($[Fe^{III}(ls)Fe^{III}(ls)Fe^{III}(ls)]^{3+}$). Complex **1a** represents a simple case with only one paramagnetic Cr^{III} ion ($[Fe^{II}(ls)Cr^{III}Fe^{II}(ls)]^{2+}$) and an $S_t = {}^3/_2$ ground state.

The most important result of this study is the discovery that complete quantum mechanical delocalization of the excess electron in the mixed valent species **1b** and **3b** is possible over the *three* metal ions in the dications. This has been explained by a double exchange mechanism where the $a_1\cdots a_1$ pathway leads to ground states with maximum spins of $S_t = 2$ and $S_t = 1$, respectively. In **2b** the $a_1\cdots a_1$ pathway is electronically blocked by a low-spin d^6 electron configuration of the central

(106) Hubbard, J. *Proc. R. Soc. London, A* **1963**, *276*, 238.
(107) Anderson, P. W. *Rev. Mod. Phys.* **1978**, *50*, 191−201.
(108) Wu, C.-C.; Jang, H. G.; Rheingold, A. L.; Gütlich, P.; Hendrickson, D. H. *Inorg. Chem.* **1996**, *35*, 4137.
(109) Kambara, T.; Hendrickson, D. N.; Sorai, M.; Seung, M. O. *J. Chem. Phys.* **1986**, *85*, 2895.
(110) Nakano, M.; Sorai, M.; Vincent, J. B.; Christou, G.; Jang, H. G.; Hendrickson, D. N. *Inorg. Chem.* **1989**, *28*, 4608.

Co^{III} ion, and consequently, an electron hopping process has been observed (class II behavior). Effectively, we have achieved an electronic fine-tuning of intramolecular electron transfer in this series of complexes.

Acknowledgment. We thank the Fonds der Chemischen Industrie and the German Federal Ministry for Education, Science, Research and Technology (BMBF) for financial support. Dr. Werner Klotzbücher (MPI, Mülheim) is thanked for measuring the temperature-dependent electronic absorption spectra.

Supporting Information Available: Figures S1−S13, Tables S1−S15 of crystallographic and crystal structure refinement data, atom coordinates, bond lengths and angles, anisotropic thermal parameters, and calculated positional parameters of hydrogen atoms, Table S16 of fit results of the EXAFS spectra, Table S17 of XANES results, and Table S18 of electronic spectra (PDF, CIF). This material is available free of charge via the Internet at http://pubs.acs.org.

JA982898M